Applied Energy 388 (2025) 125622

Contents lists available at ScienceDirect

Applied Energy

journal homepage: www.elsevier.com/locate/apenergy

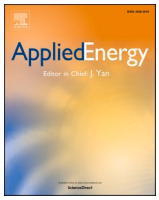

Carbon dioxide as cushion gas for large-scale underground hydrogen storage: Mechanisms and implications

Peng Deng [a,b], Haoming Ma [b], Jinghan Song [c], Xiaolong Peng [a], Suyang Zhu [a], Dan Xue [b], Liangliang Jiang [b,*], Zhangxin Chen [d,e,b,**]

[a] State Key Laboratory of Oil and Gas Reservoir Geology and Exploitation, Southwest Petroleum University, Chengdu, China
[b] Department of Chemical and Petroleum Engineering, University of Calgary, Calgary, Alberta, Canada
[c] PipeChina Pipeline Technology Development Corporation, Tianjin, China
[d] Ningbo Institute of Digital Twin, Eastern Institute of Technology, Ningbo, China.
[e] College of Petroleum Engineering, China University of Petroleum, Beijing, China

HIGHLIGHTS

- The PNM model was utilized to distinguish the differences in capillary force and relative permeability between H_2 and CO_2.
- An enhanced reservoir numerical simulation model accounted for the property differences between H_2 and CO_2.
- A detailed mechanistic analysis of interfacial tension, capillary force, relative permeability, density, and viscosity has been conducted for CO_2 as cushion gas.
- CO_2 can form a low-mobility barrier between water and hydrogen, offering significant potential as a cushion gas for UHS.

ARTICLE INFO

Keywords:
Carbon dioxide utilization
Component simulation
Depleted gas reservoir
Hydrogen storage
Pore network model
Water intrusion

ABSTRACT

The unique properties between hydrogen and water, such as high interfacial tension and capillary force, pose a significant risk of water intrusion in large-scale Underground Hydrogen Storage (UHS). With the utilization of the Pore Network Modeling (PNM) and reservoir numerical simulation methods, this study investigates the mechanisms and implications of using CO_2 as cushion gas in UHS to promote efficient injection and production, with high recovery factors and low volumes of water production. Under a realistic geological condition of the Yakela gas reservoir, serving as a geological reference, the PNM indicates a considerable decrease in capillary force, and an appreciable increase in relative permeability after injection of CO_2 cushion gas in UHS. Furthermore, a reservoir numerical mechanistic model shows that the CO_2 cushion gas established a special protection zone at the leading edge of the hydrogen storage zone, characterized by low interfacial tension, high viscosity, and density. In a realistic model application in the Yakela gas reservoir, the use of 30 % CO_2 as cushion gas leads to a significant reduction in water cut, dropping from 28 % to 8 %. Additionally, the period of stable production is extended to 5.5 months, leaving only 5.4 % of the hydrogen unrecovered following five cycles. This study highlights the significant potential of CO_2 as a cushion gas in UHS, which not only enhances the recovery factor but also provides a valuable technical reference for cushion gas selection in real-world UHS projects.

Abbreviations: b_i, Covolume parameters for the i-th component; $f_{g,i}$, Fugacity of the i-th component in the gas phase; $f_{l,i}$, Fugacity of the i-th component in the liquid phase; g_o, Gravitational acceleration, m/s^2; F, Geometrical size factor; g, Flow conductance; k, Rock permeability, mD; k_r, Relative permeability; K_v, Viscosity correlation factor; $L_{i\text{-}j}$, Distance between pores, m; m_i, Component-specific factor; M, Molar weight, kg/mol; p, Pressure bar; p_c, Capillary force, bar; p_{ci}, Critical pressure, bar; p_{nw}, Non-wetting phase pressure, bar; p_w, Wetting phase pressure, bar; Q, Volumetric flow rate, m^3/s; R, Pore radius, m; S_g, Gas saturation, %; S_l, Liquid saturation, %; S_w, Water saturation, %; T_{ci}, Absolute critical temperature, °C; T_x, Modified temperature term; u_j, Darcy velocity, m/s; V, Molar volume, m^3/mol; x_i, Mole fraction in the liquid; x_v, Viscosity adjustment factor; y_i, Mole fraction in the gas phase; y_v, Viscosity exponent; α_1 and β_1, Empirical coefficient; $(a\alpha)_i$, Dimensional attraction parameter; $(a\alpha)_m$, Attraction parameter; γ, Time-related parameter; δ_{ij}, Binary interaction coefficient; ξ_g, Molar density of gas phase, mol/m^3; ξ_l, Molar density of liquid phase, mol/m^3; ξ_w, Molar density of water phase, mol/m^3; θ, Contact angle between gas and rock; μ, Viscosity, cP; ρ, Mass density, kg/m^3; τ, Interfacial tension between water and gas, mN/m; Φ, Rock porosity, %; ω_i, Pitzer's acentric factor.

* Corresponding author at: Department of Chemical and Petroleum Engineering, University of Calgary, 2500 University Drive NW, Calgary, Alberta, Canada.
** Corresponding author at: Ningbo Institute of Digital Twin, Eastern Institute of Technology, Ningbo, China.
E-mail addresses: jial@ucalgary.ca (L. Jiang), zhachen@ucalgary.ca (Z. Chen).

https://doi.org/10.1016/j.apenergy.2025.125622
Received 6 October 2024; Received in revised form 19 January 2025; Accepted 22 February 2025

1. Introduction

In response to climate change, 196 countries and organizations have joined the Paris Agreement, aiming to circumvent hazardous climate change by confining global warming to significantly below 2 °C and striving to limit it to 1.5 °C [1,2]. Since a H_2 energy chain produces little or no CO_2 emissions in its production process, the green hydrogen (electrolysis), blue hydrogen (in combination with carbon capture and storage), turquoise hydrogen (pyrolysis), and purple hydrogen (nuclear power) have been widely regarded as ideal fuels of the future, and the H_2 economy is expected to have a broad and promising future [3,4]. A future hydrogen energy chain is depicted in Fig. 1. Renewables like wind and solar power are utilized to generate electricity for powering water electrolysis in large-scale hydrogen production facilities [5]. This hydrogen is directly injected into subsurface for Underground Hydrogen Storage (UHS) and then distributed to various downstream consumers such as households, factories, automobiles, and even ships [6]. Given that a hydrogen production rate in UHS can be exceptionally high, it is capable of furnishing energy at peak demand times. In summary, this hydrogen energy chain ideally operates with minimal environmental impact, particularly with hydrogen production methods that result in limited or even zero CO_2 emissions, highlighting its potential in promoting a sustainable future [7].

Although the promising prospect of hydrogen as a sustainable energy source for the future, the key factor for its large-scale implementation remain ensuring a stable energy supply [9]. Since the market demand for energy varies seasonally, and plants generally aim to maintain continuous production to ensure cost-effective operation [10]. For example, the winter often represent a peak for energy demand, and summer is typically an off-peak season. However, continuous production at the plant is preferred to reduce electricity production costs by up to 17.5 % [10]. Overall, the UHS technology can play a significant role in the future hydrogen market by storing excess hydrogen in the summer and supporting the rapid demand in the winter, thereby achieving energy demand peak-shifting to meet market requirements [11].

Typically, three types of UHS facilities prevail: depleted gas reservoirs, salt caverns and aquifers, as shown in Table 1. For the salt cavern storage type, fresh water is injected to dissolve the solid salt and form a cavern. This process takes a long time, typically lasting 2 to 5 years. Additionally, the volume of salt caverns is usually limited, depending on the stability of the salt formation, with each cavern generally ranging from one hundred thousand to one million cubic meters [12–14]. As for the aquifer storage type, the storage capacity can be much higher than that of salt caverns, generally reaching up to billions of cubic meters. For example, the Stenlille aquifer gas storage in Denmark can hold three billion cubic meters [15]. However, aquifer storage is seldom used for underground storage because key parameters such as the seal integrity of the cap rock, the active pressure of faults, and the effective gas storage boundary are all filled with uncertainties, making the completion of such projects highly challenging [16,17].

As for the depleted gas reservoir storage type, there are several advantages, such as high permeability and a well-defined understanding of a geological structure after decades of natural gas production. Furthermore, recent studies report that the gas reservoir's cap rock has strong sealing ability for hydrogen, as hydrogen has much higher interfacial tension than natural gas, resulting in higher capillary pressure [18]. Moreover, recent molecular simulation results show that a water film can be formed between hydrogen and the cap rock, further preventing hydrogen leakage [19]. These studies suggest that if the cap rock can

Table 1
Selected global planned large-scale UHS facilities [20].

Type	Project name	Country	Project start year	Working storage (GWh)	Status
Depleted gas reservoir	CO_2 CRC H_2 storage	Australia	mid-2020s	–	CS
	Dolni dunaiovice	Czech	–	–	CS
	Rehden	Germany	–	10,725	CS
	Aquamarine	Hungary	2025	–	UC
	Green hydrogen @ Kinsale	Ireland	2030s	3000	FS
	Storage hub italy	Italy	–	–	CS
	Humber hydrogen storage	United Kingdom	2028	320	FS
	Green hydrogen hub	Denmark	2025	250	FS
Cavern	Jemgum storage	Germany	mid-2020s	250*	CS
	H_2Cast etzel	Germany	2022	230*	UC
	HyStock zuidwending	Netherlands	2027	165*	FID
	Energiepark bad Lauchstädt	Germany	2027	150	FS
Aquifer	Lacq hydrogen	France	2030s	–	CS

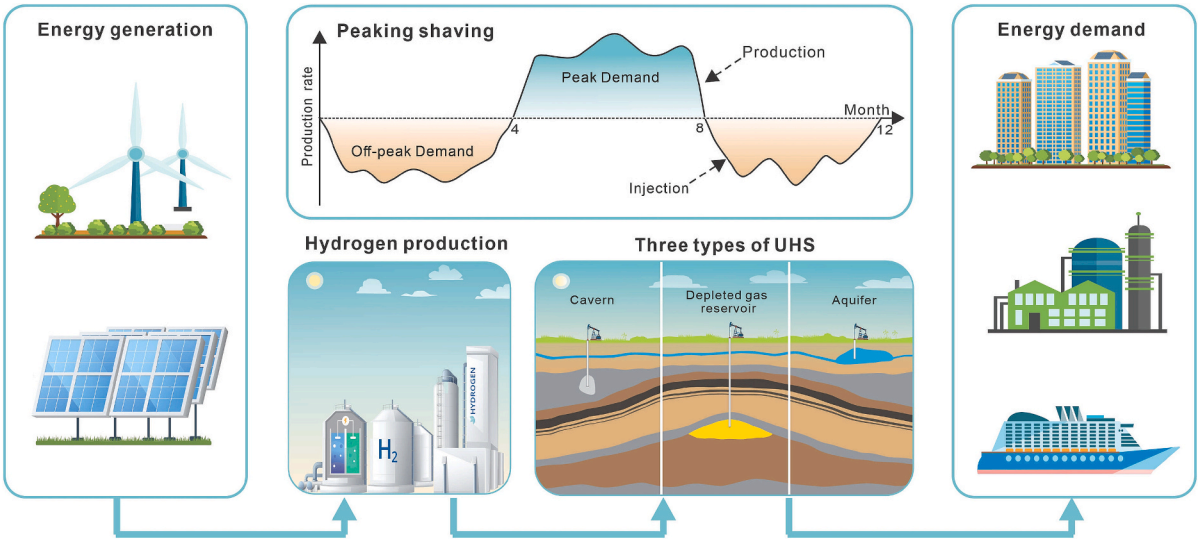

Fig. 1. A hydrogen energy chain in the future [2,5,8].

seal natural gas, it can also effectively seal hydrogen. Additionally, since the vast porous space exists in the depleted gas reservoir, the storage capacity can be several times that of the salt cavern; for example, the Suqiao UGS storage capacity can reach approximately 4.6 billion cubic meters, and the Hutubi UHS in China has a capacity of over 11.7 billion cubic meters [12].

where " * " indicates the capacity per cavern, acknowledging that more than one cavern may eventually be built. UC = Under Construction. FID = Final Investment Decision. FS = Feasibility Study. CS = Concept Stage.

Compared to the development of Underground natural Gas Storage (UGS), UHS systems in depleted gas reservoirs consistently face challenges, such as, reduced mobility and prevalent water intrusion [21–23]. In contrast to natural gas, significant interfacial tension exists between hydrogen and water. In addition, the difference in contact angles between hydrogen and natural gas is minimal, resulting in hydrogen exhibiting greater capillary forces with water in porous structures compared to natural gas [24,25]. This variation consequently contributes to enhanced flow resistance and reduced relative permeability. In addition, during the production cycle of UHS, the increased capillary force with hydrogen enhances the pressure difference at gas-water interfaces, leading to water encroachment and infiltration into the hydrogen storage zone. Consequently, since the water phase generally serves as the wetting phase, this phenomenon tends to obstruct hydrogen flow channels and cause a water-lock challenge within the well [26]. As a result, roughly 5 % to 50 % of the injected gas can become trapped in geological formations [27]. Therefore, large-scale hydrogen storage in depleted gas reservoirs necessitates the exploration of an efficient cushion gas [28]. The cushion gas should be injected to establish an isolation zone between the aquifer and the hydrogen storage zone, effectively reducing water intrusion. For this purpose, the cushion gas should possess low mobility, such as higher density and viscosity compared to hydrogen, to form an effective barrier and reduce the risk of water encroachment into the core storage area.

Since Carbon Capture, Utilization, and Storage (CCUS) is widely regarded as an important tool for achieving global climate goals, several CO_2 capture projects from air or flue gas have been developed in recent years [29]. Employing this captured CO_2 as a cushion gas in UHS could serve as an effective approach for CO_2 utilization and storage [30]. This strategy can play a key role in helping curb greenhouse gas emissions and combat global climate change. Moreover, recent research has explored the feasibility of using CO_2 as a cushion gas in UHS. Some studies have concluded that CO_2 does not chemically react with hydrogen in gas reservoirs, primarily due to the absence of necessary conditions, such as the lack of a catalyst and high temperature above 200 °C [31]. In general, these conditions are difficult to meet within reservoirs, which suggests that the potential of CO_2 as a cushion gas is worth further investigation.

Several studies have analyzed the impact of CO_2 as a cushion gas in UHS facilities [32,33]. For instance, considering the filtering effects of CO_2 solubility, it has been shown that the purity of H_2 production is strongly influenced by the hydrodynamic interactions between H_2 and CO_2 [34,35]. Meanwhile, studies suggest that using CO_2 as a cushion gas can increase the average reservoir pressure. Since CO_2 has a higher molecular weight compared to H_2, it results in a larger density contrast, which intensifies the effects of gravity segregation. This causes CO_2 to become more concentrated in the upper layers of the reservoir [32]. Some research indicates that the injection of cushion gas into depleted gas reservoirs could help displace pre-existing water and methane, particularly in watered-out wells during the gas reservoir production. Furthermore, the introduction of additional gas phases enhances the expansibility of reservoir gas and liquids during production, consequently improving H_2 recovery factor in UHS [36].

In recent years, there have also been notable developments in CO_2 injection from carbon capture and storage projects due to the rapid development of these projects. For example, Andersen and Nilsen developed a coupled model considering thermal effects, addressing the temperature changes after CO_2 injection and their impact [37]. Kumar et al. developed a model for CO_2 storage in deep saline aquifers, and analyzed the impact of formation parameter changes on CO_2 storage stability [38]. Li et al. analyzed model uncertainty in large-scale CO_2 storage simulations, evaluating the influence of conceptual model uncertainty on model predictions based on boundary conditions [39]. Their results clarified the interactions between fluid driving forces, heterogeneity resolution, and boundary conditions in CO_2 storage models.

In summary, based on previous modeling efforts with CO_2, some limitations still persist in current research regarding the use of CO_2 as a cushion gas in UHS:

(1) Current numerical simulations generally proceed without considering the differences in capillary forces and relative permeability between H_2 and CO_2 [32,33,40]. Applying the same curves for both gases introduces uncertainties in evaluating the benefits of CO_2 as a cushion gas, as a 10 % variation can lead to an 18.2 % error in the results, as shown in Fig. 2.

(2) The mechanisms of CO_2 as a cushion gas have not been fully understood. Further research is needed to comprehensively analyze the impact of CO_2 on reservoir rock and formation water in UHS.

(3) There is a lack of real-world UHS pilot or demonstration projects, leaving actual performance in real-world scenarios unverified. This lack of data hinders decision-making in real-world UHS applications.

In this study, we aim to address the uncertainties by exploring in detail the feasibility of CO_2 as a cushion gas within large-scale UHS facilities. The structure of this paper is as follows: Section 2 introduces the details of the PNM method, which is used to determine the paraments of CO_2 and H_2, as well as the numerical simulation to calculate the cushion gas flow process. Section 3 introduces the geological conditions of the study area for this research; Section 4 provides a detailed mechanistic analysis of the key parameters which influence the distribution and flow process. Subsequently, a real-case gas field, the Yakela gas reservoir, is modeled with an analysis of the effects of CO_2 in a real inhomogeneous reservoir. Section 5 provides a summary of this study.

2. Methodology

This study employs two approaches, namely pore network modeling

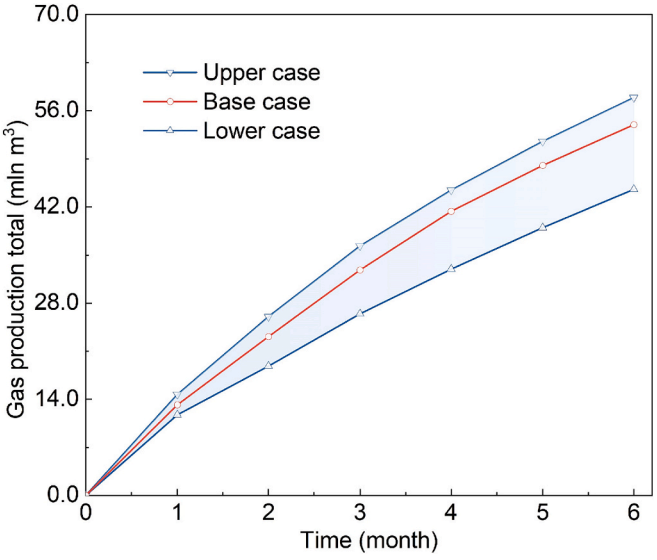

Fig. 2. The UHS simulation model showing total gas production with variations in capillary forces and relative permeability. The upper case scenario represents a 10 % increase compared to the base case, while the lower case scenario represents a 10 % decrease from the base case.

and numerical simulation, to show the mechanism and effectiveness of applying CO_2 as a cushion gas in UHS. The PNM is used to simulate the changes in capillary forces and relative permeabilities of CO_2 and H_2, as this method accounts for the differences in gas properties. Moreover, since the simulations are conducted within the same digital core sample, the results for CO_2 and H_2 provide a basis for lateral comparison. Utilizing the results of capillary force and relative permeability from the PNM, together with Yakela gas reservoir's geological data, the numerical simulation is then performed to simulate the hydrogen storage process with CO_2 as cushion gas.

2.1. Pore network model

Since there are significant differences in gas flow ability across different rock cores, it is necessary to conduct tests on the same core sample to compare the flow behavior of H_2 and CO_2. However, as the highly explosive property of H_2 requires a specialized experimental apparatus for displacement experiments, it is challenging to measure hydrogen's flow parameters in the laboratory. Additionally, comparative data for tests on the same core sample for both H_2 and CO_2 are rarely found. Hence, this study utilizes the PNM approach to simulate the transport process and to calculate the relative permeability and capillary forces of H_2 and CO_2, respectively [41].

The Hagen-Poiseuille equation is employed in the pore network modeling to compute the relationship between pressure and flow rate [42]:

$$Q = \frac{10^8 \pi R_{i-j}^4 \left(p_i - p_j\right)}{8\mu L_{i-j}} \tag{1}$$

where Q is the volumetric flow rate [m^3/s]; R is the pore radius [m]; p_i and p_j are the pressure of pores i and j [bar]; u is the viscosity [cP]; $L_{i\text{-}j}$ is the distance between pores i and j [m].

Hydraulic conductance g refers to the ability of fluid to flow through the PNM model, as defined in Eq. (2). The dynamic viscosity is represented by μ. The size factor F combines the geometrical characteristics of pore radius R and throat length L and is utilized to describe the model's geometrical characteristics:

$$g = \frac{10^3 F}{\mu} = \frac{10^3 \pi R_{i-j}^4}{8\mu L_{i-j}} \tag{2}$$

The total conductance of the pore-throat-pore system can be calculated by summing the values of three flow resistances in series: pore i (the upstream pore), throat k (the connecting conduit between the two pores), and pore j (the downstream pore). The volumetric flow rate Q is calculated as follows:

$$Q = 10^8 \left(\frac{\mu}{F_i} + \frac{\mu}{F_k} + \frac{\mu}{F_j}\right)^{-1} \left(p_i - p_j\right) \tag{3}$$

In the pore network modeling, the water phase is considered as the wetting phase, while the gas phase, including H_2 and CO_2, is the non-wetting phase. The relationship between the capillary forces P_c of the wetting and non-wetting phases is calculated using:

$$p_c = p_{nw} - p_w \tag{4}$$

where p_c, p_{nw}, and p_w are the capillary force, non-wetting and wetting phase pressure, respectively [bar].

Fig. 3 depicts the established pore network model for this study. The model includes 3216 effective pores with 1169 effective throats. To replicate the properties of the Yakela gas reservoir, the permeability and porosity of the model were calibrated to reflect the reservoir's average values, namely 35.8 mD for permeability and 13.4 % for porosity.

2.2. Numerical simulation

2.2.1. Component model

The component model is based on three fundamental governing equations: mass conservation for individual components, Darcy's law, and the Equation of State (EOS). The mass conservation equations of water and hydrocarbon components can be expressed as Eq. (5) and Eq. (6) [43–45]:

$$-\nabla\cdot(\xi_w u_w) = \frac{\partial}{\partial t}(\phi s_w \xi_w) + Q_w \tag{5}$$

$$-\nabla\cdot\left(x_i\xi_1 u_1 + y_i\xi_g u_g\right) = \frac{\partial}{\partial t}\left(\phi\left(x_i s_1 \xi_1 + y_i s_g \xi_g\right)\right) + Q_i \tag{6}$$

The Darcy's law provides the velocity of each phase [43]:

$$u_j = -\frac{10^{-7} k k_r}{\mu_j}\cdot\left[\nabla p_j - \rho_j g_o \nabla Z\right] \tag{7}$$

The equal fugacity between liquid and vapor phases is a fundamental principle in phase equilibrium thermodynamics. This assumption accounts for deviations from ideal behavior in real gases and liquids, making it more accurate than simply using pressure. According to this principle, for a given component, the fugacity in the vapor phase must

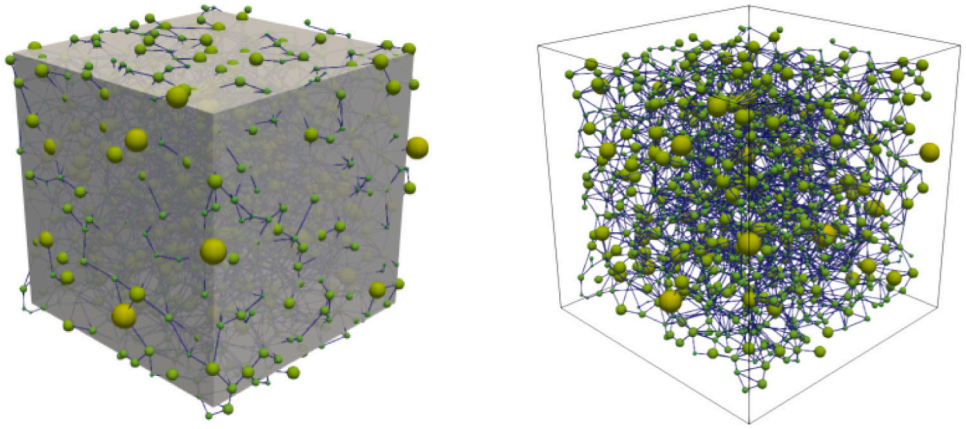

(a) (b)

Fig. 3. Pore network model structure, where green spheres represent the pores of different sizes, with 3216 effective pores ranging from 4.3 μm to 471.6 μm. The blue cylinders represent the throats connecting the pores, with a total of 1169 throats ranging from 1.2 μm to 48.6 μm. The model permeability is 35.8 mD and the porosity is 13.4 %. (a) A model showing the solid in grey to display the model's shape. (b) A model with the solid filtered out to show the detailed pore and throat connection relationships. (For interpretation of the references to colour in this figure legend, the reader is referred to the web version of this article.)

be equal to the fugacity in the liquid phase [43]:

$$f_{i,l}(p,T,x_1,x_2,\cdots,x_{nc}) = f_{i,g}(p,T,y_1,y_2,\cdots,y_{nc}) \tag{8}$$

where the subscripts w, l and g represent the water, liquid and gas phase, respectively; the subscripts i represent different components; the subscripts j signifies distinct phases; ξ represents molar density of each phase; u is the Darcy velocity [m/s]; S_g, S_l, and S_w is gas saturation, liquid saturation, and water saturation, respectively [dimensionless]; ρ is the mass density [kg/m^3]; $f_{l,i}$ and $f_{g,i}$ is the fugacity of the i-th component in the liquid and gas phase, respectively [dimensionless]; x_i and y_i respectively represent mole fraction of the i-th component in the liquid and gas phase [dimensionless]; k is rock permeability [mD]; k_r is relative permeability [dimensionless].

2.2.2. Fluid model

The EOS equation has seen significant advancements in recent years, such as in new mixtures, high-precision phase equilibrium predictions, and applications across different scales [46–48]. Despite these advancements, the Peng-Robinson (PR) EOS remains popular due to its simplicity, versatility, computational efficiency, and reasonable accuracy in predicting gas-liquid equilibria for hydrocarbons and other fluids, making it suitable for a wide range of industrial applications. The PR equation for multi-component hydrocarbon systems is as follows [49]:

$$P = \frac{(1.80T + 491.67)R}{14.5038(V - b_m)} - \frac{(a\alpha)_m}{14.5038\left(V^2 + 2b_m V - {b_m}^2\right)} \tag{9}$$

The mixture parameters $(a\alpha)_m$ and b_m are calculated based on the properties of individual components, following the mixing rules outlined below [49]:

$$(a\alpha)_m = \sum_i^{n_c}\sum_j^{n_c} c_i c_j \sqrt{(a\alpha)_i (a\alpha)_j}\left(1 - \delta_{ij}\right) \tag{10}$$

$$b_m = \sum_i^{n_c} c_i b_i \tag{11}$$

$(a\alpha)_i$ represents the dimensional attraction parameter for the i-th component in the fluid mixture, while b_i denotes the dimensional co-volume parameter for the i-th component. These parameters can be determined using Eq. (12) to Eq. (14) [48]:

$$(a\alpha)_i = 0.0315\frac{R^2[1.80T_{ci} + 491.67]^2}{p_{ci}}\left[1 + m_i\left(1 - (1.80T_{ci} + 491.67)^{0.5}\right)\right]^2 \tag{12}$$

$$b_i = \frac{R(0.14T_{ci} + 38.2519)}{14.5038p_{ci}} \tag{13}$$

$$m_i = \begin{cases} 0.3746 + 1.5423\omega_i - 0.2699\omega_i^2 & (\omega_i \le 0.49) \\ 0.3796 + 1.4851\omega_i - 0.1644\omega_i^2 + 0.017\omega_i^3 & (\omega_i > 0.49) \end{cases} \tag{14}$$

where V is the molar volume [m^3/mol]; δ_{ij} is the binary interaction coefficient between the i-th and j-th components, and $\delta_{ii} = 0$; T_{ci} is the absolute critical temperature of the i-th component [°C]; p_{ci} is the critical pressure of the i-th component [bar]; ω_i is the Pitzer's acentric factor [dimensionless].

This study established two numerical models in accordance with the geological conditions of the Yakela gas reservoir. The detailed parameters are presented in Table 2. The mechanistic model (box model), as shown in Fig. 4(a), was developed to analyze the changes in key parameters following CO_2 injection, including interfacial tension, density, and viscosity. Since this model is simple and homogeneous, it helps minimize interference from other factors, such as heterogeneities in permeability and, porosity, and an uneven distribution of water bodies. The realistic model (geological model) accurately represents the gas cap structure, heterogeneity, water body characteristics, and well injection capacity, helping to simulate the actual flow behavior and effects of CO_2 cushion gas, as shown in Fig. 4(b).

3. Study area

The Yakela gas reservoir (see Fig. 5) is located in the Tarim Basin, China. It covers an area of 65 km^2, including a hydrocarbon zone about 22 km in length and 5 km in width, covering approximately 38 km^2 [50]. The reservoir's gas layer thickness is average 31.9 m, and the pressure drops from initial 58.7 MPa to 42 MPa. The rock fracture pressure is 72 MPa, which means there is a broad range of pressure fluctuation.

The reservoir rocks, primarily composed of fine-grained feldspathic lithic sandstone, with minor amounts of feldspar quartz sandstone and mudstone, showcase a primary porosity range from 11.5 % to 15.5 %, with a mean value of 13.4 %. The irreducible water saturation are about 20.4 %. With a capacity of more than 20 billion cubic meters (BCM), the recovery factor has reached 70 %. However, due to water encroachment, many gas wells have been forced to shut down. Additionally, the reservoir features moderate permeability, mainly within the 10.1–70.6 mD range, averaging 35.8 mD. The average transmissivity is 1575.2 mD·m [51]. In the stage of natural gas production, the single well could achieve a maximum daily naturtal gas production rate of 0.6 mln m^3/d. These attributes indicate significant potential for increased storage capacity and improved flow performance upon conversion to a UHS in the future.

The Yakela reservoir comprises three gas layers: the upper (13 m), middle (11 m), and lower (20 m), separated by two main cap layers and a thin intermediate layer [51]. The upper and middle gas layers are completely sealed by a thick layer of reddish-brown mudstone interbedded with grayish-white siltstone, with a thickness ranging from 107 m to 726 m. However, the intermediate layer between the middle and lower gas layers is discontinuous, rendering the middle and lower gas layers interconnected. Dynamic production analysis indicates that the upper gas layer is sufficiently isolated from the below layers, operating as two distinct reservoirs.

Even though the Yakela gas reservoir is at a greater depth than the typical UHS depth, there are several advantages to select it as the UHS case study. For example, deep storage facilities offer a higher production rate due to its ability to operate at higher pressures. Additionally, exploring the feasibility of UHS in deep formations expands the potential storage zones for UHS facilities, helping to ensure a broader supply in the future hydrogen energy society.

Based on the previous introduction, there are several advantages for the Yakela gas reservoir to be converted for UHS: its thick caprock

Table 2
Basic parameters of two models.

Reservoir property	Value (*min*-max, *mean*)	Unit
Reservoir area	38.6	km^2
Depth	5200–5400	m
Initial pressure	587	bar
Thickness	17.0–46.0, 31.9	m
Initial reservoir temperature	134.1	°C
Water saturation	20.4–82.1, 67.2	%
Porosity	11.5–15.5, 13.4	%
Permeability	10.1–70.6, 35.8	mD
Rock compressibility	1.4×10^{-6}	bar^{-1}
Gridding size - I, J, K (Mechanistic model)	$10 \times 10 \times 0.2$	m
Total grid number (Mechanistic model)	1.8×10^4	Dimensionless
Gridding size - I, J, K (Realistic model)	$25 \times 25 \times 1$	m
Total grid number (Realistic model)	202×10^4	Dimensionless

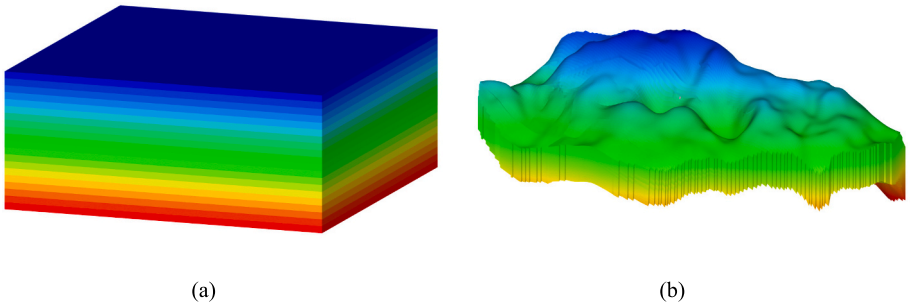

(a) (b)

Fig. 4. Numerical simulation models in this study. (a) Mechanistic model (box model). (b) Realistic model (geological model).

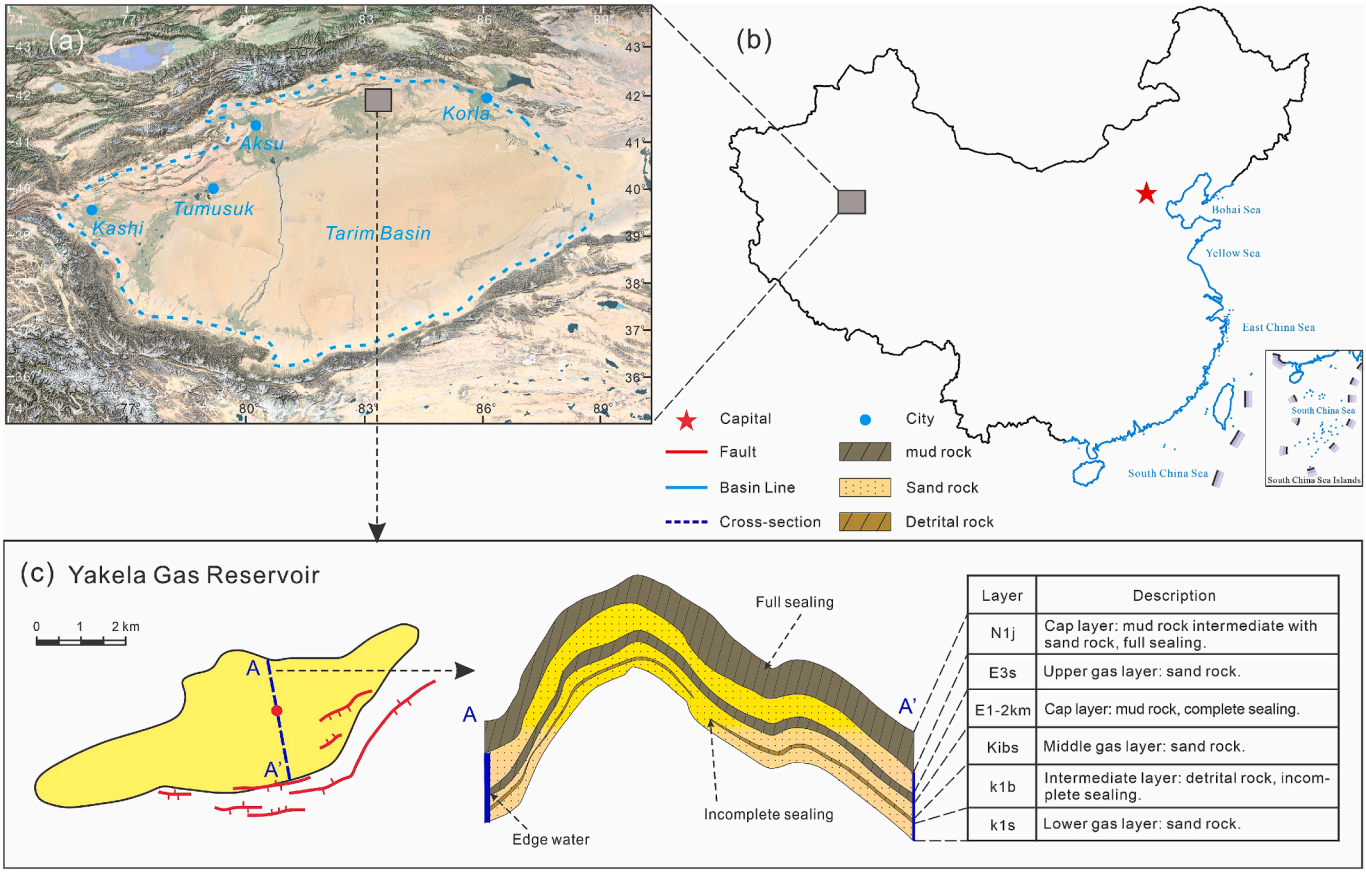

Layer	Description
N1j	Cap layer: mud rock intermediate with sand rock, full sealing.
E3s	Upper gas layer: sand rock.
E1-2km	Cap layer: mud rock, complete sealing.
Kibs	Middle gas layer: sand rock.
k1b	Intermediate layer: detrital rock, incomplete sealing.
k1s	Lower gas layer: sand rock.

Fig. 5. Tarim Basin and Yakela Gas Reservoir. (a) Satellite imagery of the Tarim Basin, sourced from Google Maps; (b) Map of China, sourced from the Ministry of Natural Resources of the People's Republic of China; (c) Stratigraphic profile data of the Yakela Gas Reservoir [52,57].

ensures good sealing performance for hydrogen, its relatively few faults reduce the risk of gas leakage through fault activation, and its highly homogeneous layer contributes to a uniform distribution of H_2 within the reservoir.

Significant water intrusion is the main challenge in the Yakela gas reservoir. As a result, the water cut in most wells exceeds 70 %, leading to the shutdown of production wells. It is therefore crucial to consider the impacts of water drive during the UHS phase. This study proposes the utilization of CO_2 as a cushion gas for hydrogen storage, with the objective of enhancing the operational efficiency of UHS.

4. Results and analysis

4.1. Model validation

To validate the model's effectiveness, this study conducted history matching using 18 years of production data from Well A in the Yakela gas reservoir, as shown in Fig. 6. The numerical simulation model achieved a Mean Absolute Error (MAE) of 9.6 % for gas production rates and 7.5 % for water production rates compared to historical data. Since numerical simulations with MAE below 10 % are generally considered representative of real conditions, these results indicate that the model can accurately simulate the reservoir flow behavior.

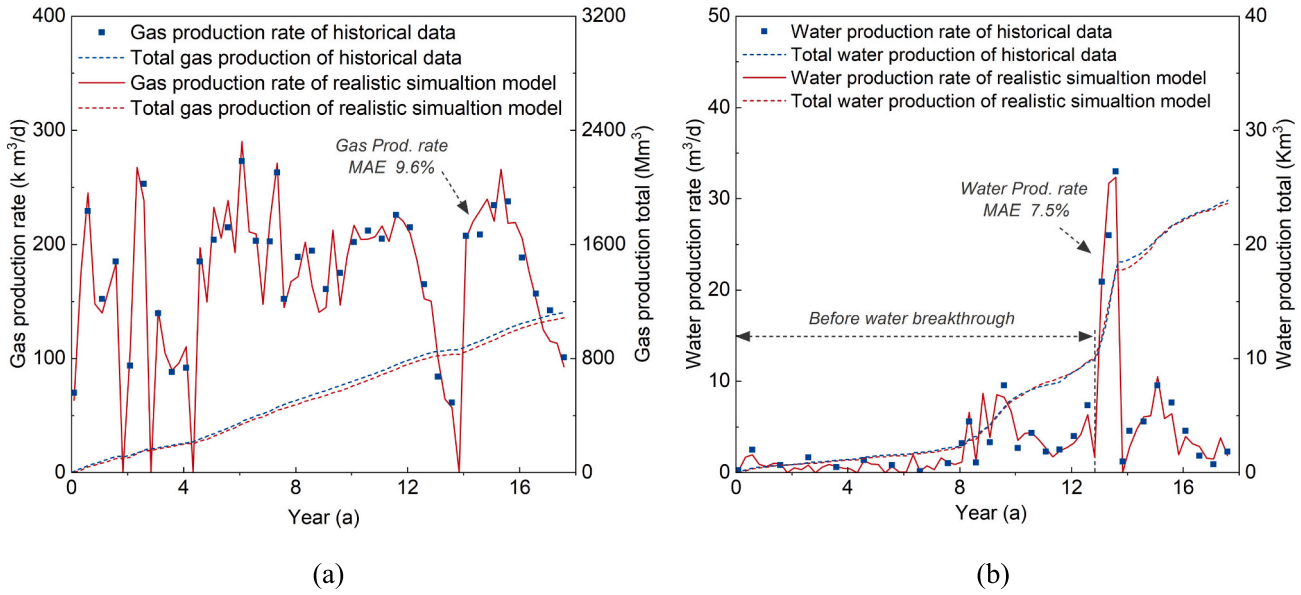

Fig. 6. Production history matching data of Well A. (a) The gas production rate and total production. (b) The water production rate and total production, where MAE refers to mean absolute error.

4.2. Mechanistic analysis

The use of CO_2 as cushion gas introduces several effects on UHS performance, including the reduction of interfacial tension, decline of capillary forces, enhancement of relative permeability, and the generation of both high-density and high-viscosity isolation zones. These specific impacts were analyzed in detail through the following research.

4.2.1. Interfacial tension reduction

Interfacial tension significantly influences gas-liquid interface distribution. Research has shown that elevated interfacial tension may yield higher capillary forces, which can initiate water fingering during gas-liquid interface displacement, thereby reducing H_2 recovery efficiency. The interfacial tension, which depends on the fluid's density difference and critical temperature, can be calculated using Eq. (15) to Eq. (17) [53].

$$\gamma^{1/4} = \frac{\alpha_1 \Delta\rho^{\beta_1}}{T_x^{0.3125}} \tag{15}$$

with

$$T_x = \frac{T}{185.78 \times (\Delta\rho)^{-0.569}} \tag{16}$$

where

$$\Delta\rho = |\rho_w - \rho_g| \tag{17}$$

The coefficients a_1 and b_1 can be derived from Eq. (18) and Eq. (19).

$$\alpha_1 = \begin{cases} 2.2062 & (\Delta\rho \le 0.2) \\ 2.9150 & (0.2 < \Delta\rho \le 0.5) \\ 3.3858 & (0.5 < \Delta\rho \le 0.75) \\ 3.3178 & (\Delta\rho > 0.75) \end{cases} \tag{18}$$

$$\beta_1 = \begin{cases} -0.94716 & (\Delta\rho \le 0.2) \\ -0.76852 & (0.2 < \Delta\rho \le 0.5) \\ -0.6290 & (0.5 < \Delta\rho \le 0.75) \\ -0.6980 & (\Delta\rho > 0.75) \end{cases} \tag{19}$$

where γ is a time-related parameter; ρ is the mass density; α_1 and β_1 are empirical coefficients determined from experimental data; T is the temperature at the calculation point; T_x is a modified temperature term that takes into account the density difference between the two phases.

The interfacial tension variability between hydrogen and CO_2 with water across a temperature range of 87 °C to 150 °C for different mixture ratios are shown in Fig. 7. The figure shows a consistent decrease in the interfacial tension as temperature and pressure rise. However, the interfacial tension between hydrogen and water shows a negligible response to pressure changes. At 87 °C, a pressure increase from 100 to 800 bar results in only a 0.4 mN/m decrease in interfacial tension. In contrast, with the same pressure range, the interfacial tension between CO_2 and water significantly diminishes, resulting in a reduction of 23.3 mN/m. For a H_2 and CO_2 mixture, increasing the proportion of CO_2 leads to a significant decrease in interfacial tension. The results show that introducing CO_2 as a cushion gas in UHS reduces interfacial tension, thereby influencing the balanced distribution of gas and water.

The mechanistic model showing a hydrogen injection of 0.4 pore volumes (PV) with varying CO_2 proportions is depicted in Fig. 8. The first row illustrates a scenario without CO_2 injection. Where the hydrogen region with high interfacial tension directly interfaces with the other phase. The second to the fourth rows display hydrogen injection scenarios with a CO_2 cushion gas ranging from 15 % to 45 %. In these cases, a low interfacial tension isolation zone emerges ahead of the high hydrogen interfacial tension region, potentially reducing interfacial tension by up to 44.5 %. Due to the presence of water in the bottom layer, this low interfacial tension zone expands. Furthermore, the zone expands significantly as the number of injection cycles increases.

Since low interfacial tension contributes to stabilizing the gas-water interface, the low interfacial tension zone in the UHS helps reduce the viscous fingering phenomenon, especially during the H_2 production stage. As a result, this low interfacial tension zone promotes the stability of the hydrogen storage zone. As the Fig. 8 shows, when the CO_2 proportion exceeds 30 %, the low interfacial tension increases significantly. Therefore, from the perspective of interfacial tension, a CO_2 proportion around 30 % suffices.

4.2.2. Capillary force decline

This study utilized a PNM to simulate the capillary forces of H_2 and CO_2 within a shared core sample. To reflect the actual conditions of the formation in the Yakela gas reservoir, the core sample's temperature, pressure, porosity, and permeability were adapted according to the Yakela gas reservoir parameters in Table 2. The capillary forces P_c can be

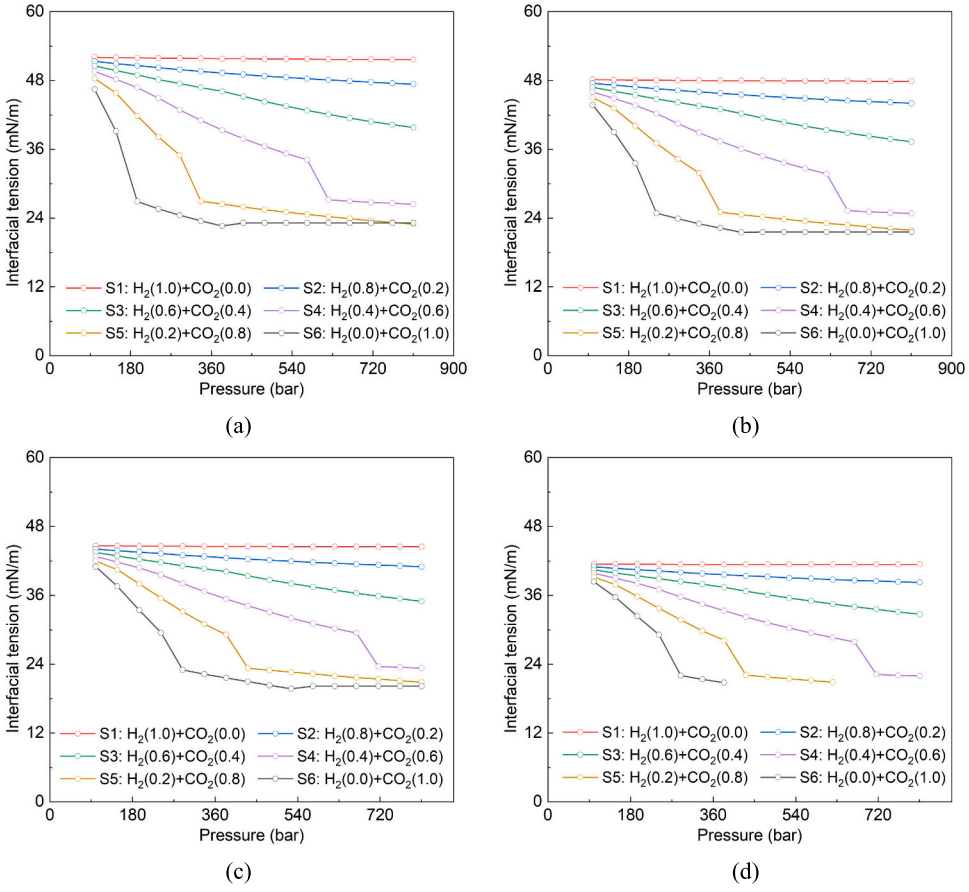

Fig. 7. Interfacial tension variability between hydrogen and CO_2 with water for different mixture ratios. (a) Temperature at 87 °C. (b) Temperature at 107 °C. (c) Temperature at 128 °C. (d) Temperature at 150 °C.

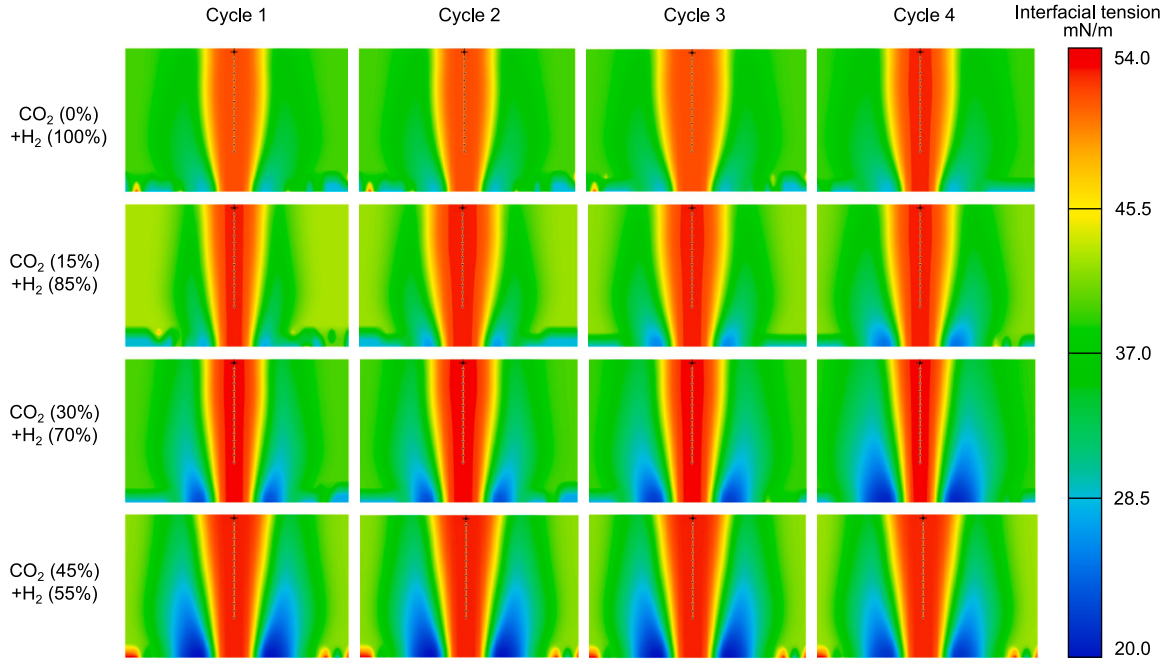

Fig. 8. Interfacial tension of H_2 injection with CO_2 as cushion gas in mechanistic model.

obtained from Eq. (20):

$$p_c = \frac{2\tau cos\theta}{r} \tag{20}$$

where τ is the interfacial tension between water and gas [mN/m]; θ is the contact angle between gas and rock [dimensionless].

The capillary force distribution model for water displacement by H_2 and CO_2 at the point of completion is shown in Fig. 9. The properties of H_2 and CO_2 significantly influence the capillary force distribution within the rock core. Due to these properties, minimal overlap is observed between H_2 and CO_2. At the displacement endpoint, the capillary force distribution for H_2 across various pores ranges from 13 to 18 bar, while for CO_2, it ranges between 4 and 6 bar.

The entire capillary force curve in the PNM during displacement by H_2 and CO_2 is shown in Fig. 10. There are three stages for the gas invasion process. The first one is the initial entry stage, where the gas invades the largest pores. The initial entry pressure P_e is 2.3 bar and 0.8 bar for H_2 and CO_2 respectively. After that, the expansion stage is the invasion in the medium-sized pores, which occupy the majority of the pore space and result in a gradual change in capillary pressure. The last stage is the invasion in the micropores, resulting in a rapid increase in the capillary force. The maximum displacement pressure p_{max} is 18.1 bar and 6.6 bar for H_2 and CO_2, respectively. Thus, incorporating CO_2 as a cushion gas in UHS can significantly reduce capillary forces throughout the gas injection process. This reduction helps mitigate the water fingering phenomenon, prevents the formation of rapid water channels, and reduces the risk of water flooding in production wells.

4.2.3. *Relative permeability enhancement*

In contrast to permeability, which is an intrinsic property of the rock, relative permeability is influenced by capillary force, viscosity, fluid density, and other fluid properties. A preliminary characterization of H_2 and CO_2 highlights that while hydrogen's lower viscosity promotes fluid flow, its higher capillary force may offset this mobility advantage. As a result, this study employs the PNM to distinguish the unique features of the relative permeability curves for H_2 and CO_2. In this model, the flow rate, as shown by Eq. (21), plays a crucial role in the computation of relative permeability. The procedure begins by computing the absolute flow rate of a single-phase fluid traversing the core. Subsequently, the relative flow rate is calculated under gas-displacing-water conditions, and the ratio of these two values determines the relative permeability.

$$k_r = \frac{k_e}{k_{abs}} = \frac{Q_e}{Q_{abs}} = \frac{u_e}{u_{abs}} \tag{21}$$

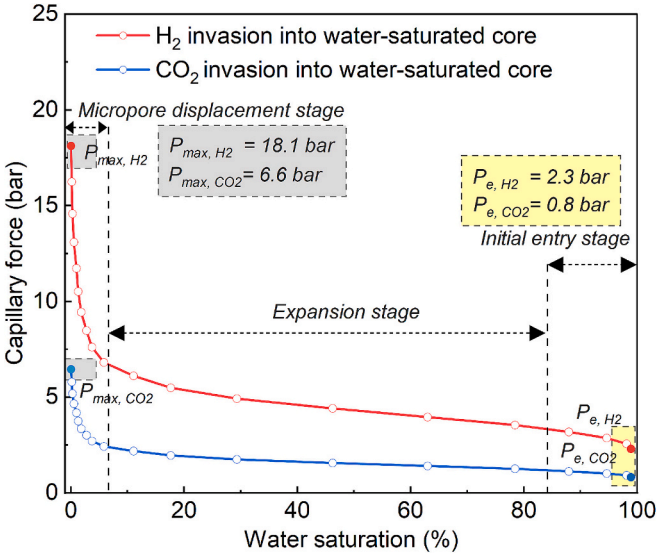

Fig. 10. Capillary force curves under different displacing gases.

where k is permeability, k_r is the relative permeability, and subscripts 'e' and 'abs' denote effective and absolute, respectively.

where k is permeability; kr is relative permeability; the subscripts 'e' and 'abs' represent 'effect' and 'absolute', respectively.

The entire displacement process, involving varying relative velocities of H_2 and CO_2, is shown in Fig. 11. From the figure, the results show a significant difference in relative velocity between H_2 and CO_2 in most of the pores, with only a small number of highly connected pores consistently maintaining high relative velocity after the displacement begins. Moreover, H_2 consistently exhibits lower flow capacity than CO_2 across different displacement stages. This indicates that CO_2 shows higher permeability and mobility in UHS reservoirs. The main difference between H_2 and CO_2 lies in their flow behavior within small pores. As a result, CO_2 can migrate through pores of varying sizes and connectivity more effectively.

The relative permeability curves of H_2 and CO_2 for the entire displacement process are shown in Fig. 12. It can be observed that hydrogen's relative permeability is significantly lower than that of CO_2, as gas velocity is influenced by viscosity and pressure gradient according to Darcy's law. Although H_2 has a much lower viscosity than CO_2, which is advantageous for flow in the reservoir, the relative permeability test

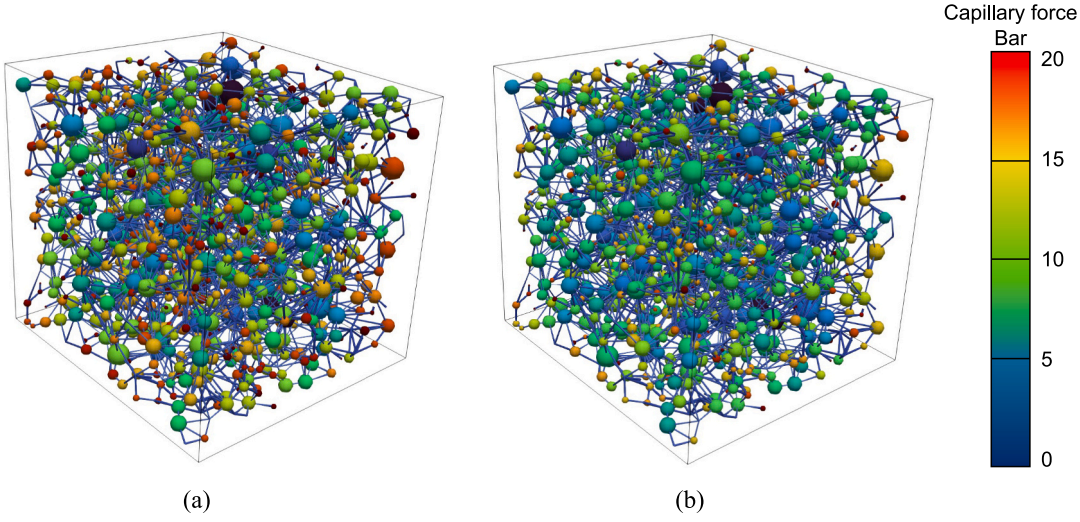

Fig. 9. 3D visualization of capillary forces under different displacing gases. (a) H_2 displacing water model. (b) CO_2 displacing water model.

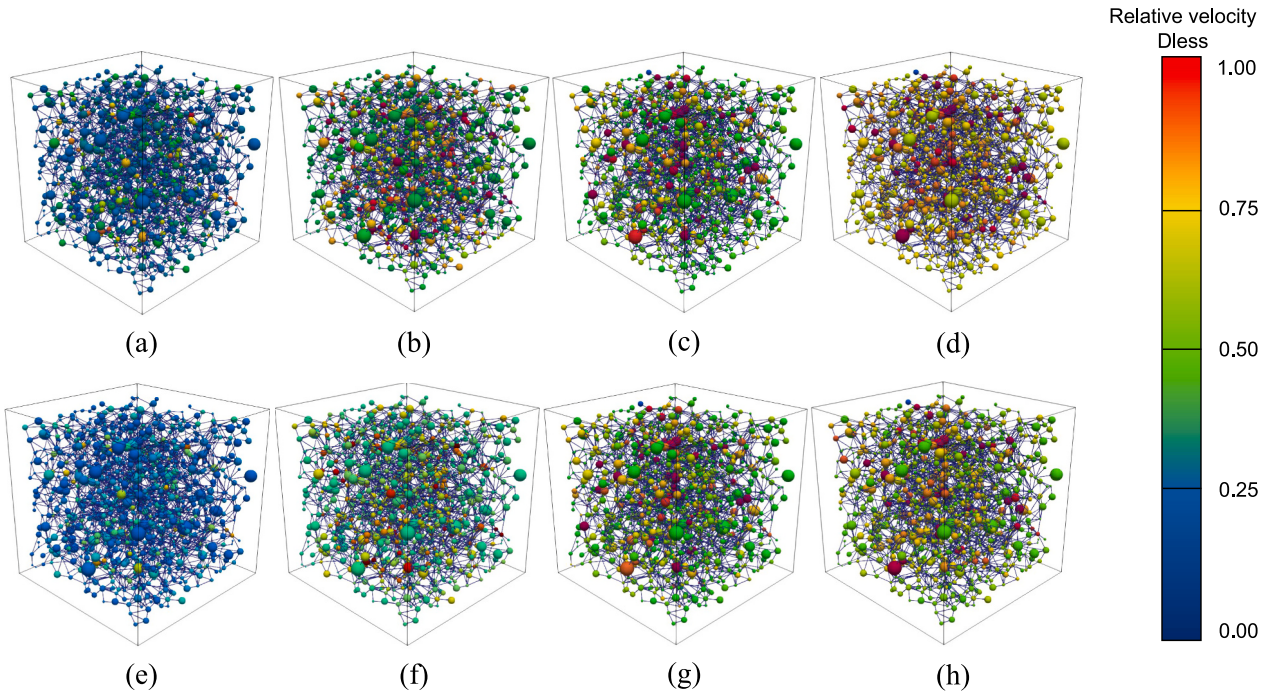

Fig. 11. Relative velocities of H_2 and CO_2 under various saturations. (a)-(d) depict the relative velocity of CO_2 at saturations of 20 %, 40 %, 60 %, and 80 %, respectively; (e)-(h) represent the relative velocity of H_2 at the same saturations. Where dless means dimensionless.

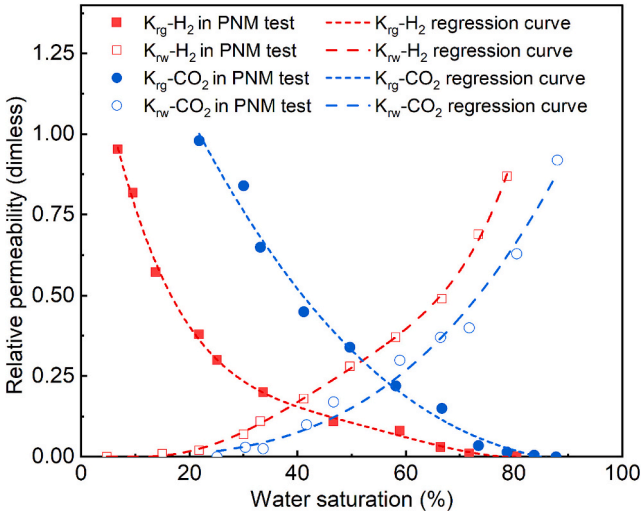

Fig. 12. Relative permeability curves under different displacing gases.

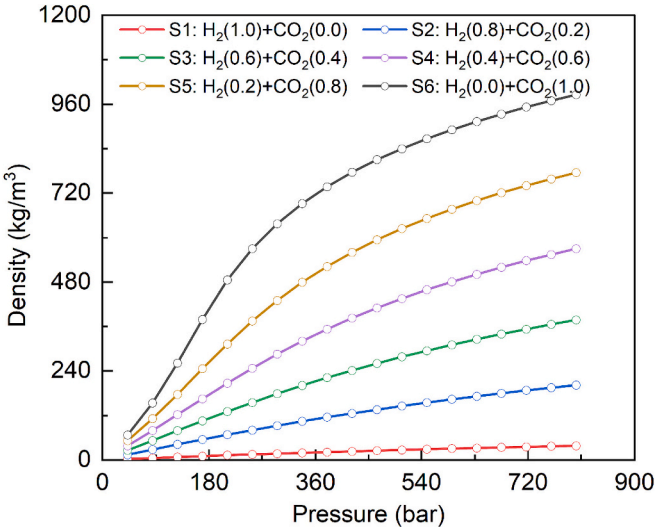

Fig. 13. Density curves for H_2 and CO_2 at varying mixing ratios as a function of pressure.

results in Fig. 12 indicate that this advantage is counteracted by capillary forces, resulting in the relative permeability of H_2 being relatively lower. Furthermore, the flow of H_2 gas exhibits distinct stages: it is slow at water saturations above 30 %, below which the flow capacity increases rapidly as water saturation decreases.

4.2.4. *High-density isolation zone generation*

Since density plays a crucial role in the distribution of mixed fluids, and there is a significant difference in the densities between natural gas, CO_2, and H_2. As a result, the distribution pattern of mixed gases after CO_2 been injected in UHS should be studied. The relationship between density and pressure for H_2 and CO_2 at various mixing ratios is shown in Fig. 13. The density of hydrogen displays relative stability with a modest increase from 26 to 38 kg/m^3 as pressure increases from 50 to 800 bar. In contrast, the density of CO_2 exhibits a significant increase, soaring from 67 to 985 kg/m^3. A similar pattern is observed in the mixed hydrogen and CO_2 gas, where the density gradually increases to values within the range of those for pure CO_2 as the CO_2 mixing ratio increases.

Water intrusion can significantly influence the stable operation of the hydrogen storage facility. The injection of CO_2 as a cushion gas is beneficial in forming a isolation zone at the outer boundary of the hydrogen zone, thereby reduce the influence of bottom water on the UHS stability. Fig. 14 illustrates the density distribution in the box model using different proportions of CO_2, ranging from 0 to 45 %, as the cushion gas. As the injection ratio of CO_2 increases, a clearly delineated high-density isolation zone develops in the leading edge of the hydrogen storage area. This isolation zone becomes more pronounced with increasing CO_2 injection ratios and with each additional cycle. When the proportion of CO_2 reaches 30 %, an zone nearly approaching the

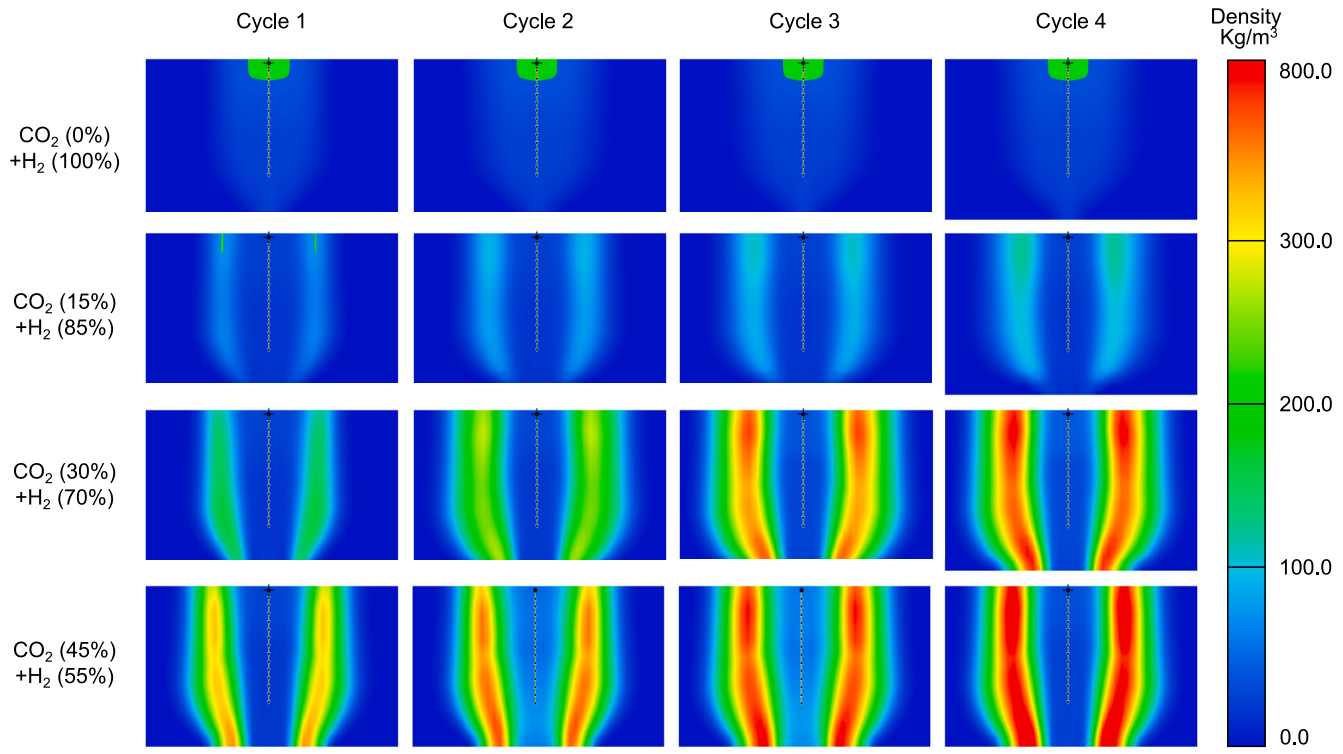

Fig. 14. Density of hydrogen with CO_2 as cushion gas in mechanistic model.

maximum density of pure CO_2 under these pressure and temperature conditions can be generated, which provides significant isolation between H_2 and water.

4.2.5. *High-viscosity isolation zone formation*

Just as Darcy equation given in Eq. (7), viscosity plays a crucial role in the flow process for UHS. Eq. (22) to Eq. (25) show the gas viscosity can be calculated with Lee-Gonzalez-Eakin method [54,55].

$$\mu_g = 1.10^{-4} k_v EXP\left(x_v \left(\frac{\rho_g}{62.4}\right)^{y_v}\right) \tag{22}$$

where

$$k_v = \frac{(9.4 + 0.02MW_g)T^{1.5}}{209 + 19MW_g + T} \tag{23}$$

$$y_v = 2.4 - 0.2x_v \tag{24}$$

$$x_v = 3.5 + \frac{986}{T} + 0.01MW_g \tag{25}$$

where K_v is a viscosity correlation factor; x_v is a viscosity adjustment factor; y_v is a viscosity exponent; μ_g *is* the gas viscosity; MW_g *is the* molecular weight of gas.

The correlation between the viscosities of hydrogen and CO_2 across various mixing ratios is shown in Fig. 15. Within a pressure scope from 50 to 800 bar, the viscosity of pure hydrogen manifests a minor increase, transitioning from 0.009 to 0.012 cP. In contrast, the viscosity of pure CO_2 undergoes a more pronounced change, rising from 0.020 to 0.107 cP. For mixed gases, there's a consistent rise in viscosity as the proportion of CO_2 in the mixture increases, trending towards the viscosities of pure hydrogen and CO_2.

The viscosity profiles of hydrogen injection within the mechanistic model, which includes varying proportions of CO_2 as a cushion gas are shown in Fig. 16. The injection of CO_2 influences the model to produce a high-viscosity region near the injection well's base. As the quantity of

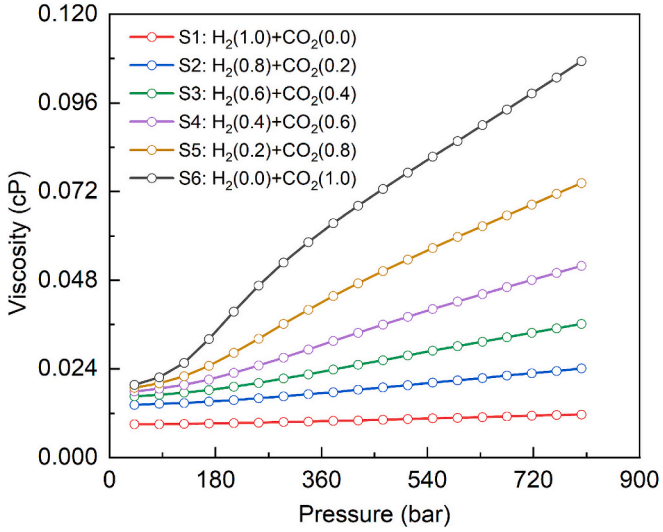

Fig. 15. Viscosity curves for H_2 and CO_2 at varying mixing ratios as a function of pressure.

injected CO_2 increases, the height and breadth of this high-viscosity region expand correspondingly. According to Darcy's law, as depicted in Eq. (7), the fluid viscosity is inversely proportional to the flow rate of the fluid. Consequently, the high-viscosity region forming near the well's base reduces the flow velocity, creating a flow barrier between the aquifer and the hydrogen storage core zone, thereby preventing water intrusion into UHS facilities.

4.3. *Case study*

Utilizing the realistic model of the Yakela gas reservoir, this study developed and evaluated four hydrogen injection strategies. The

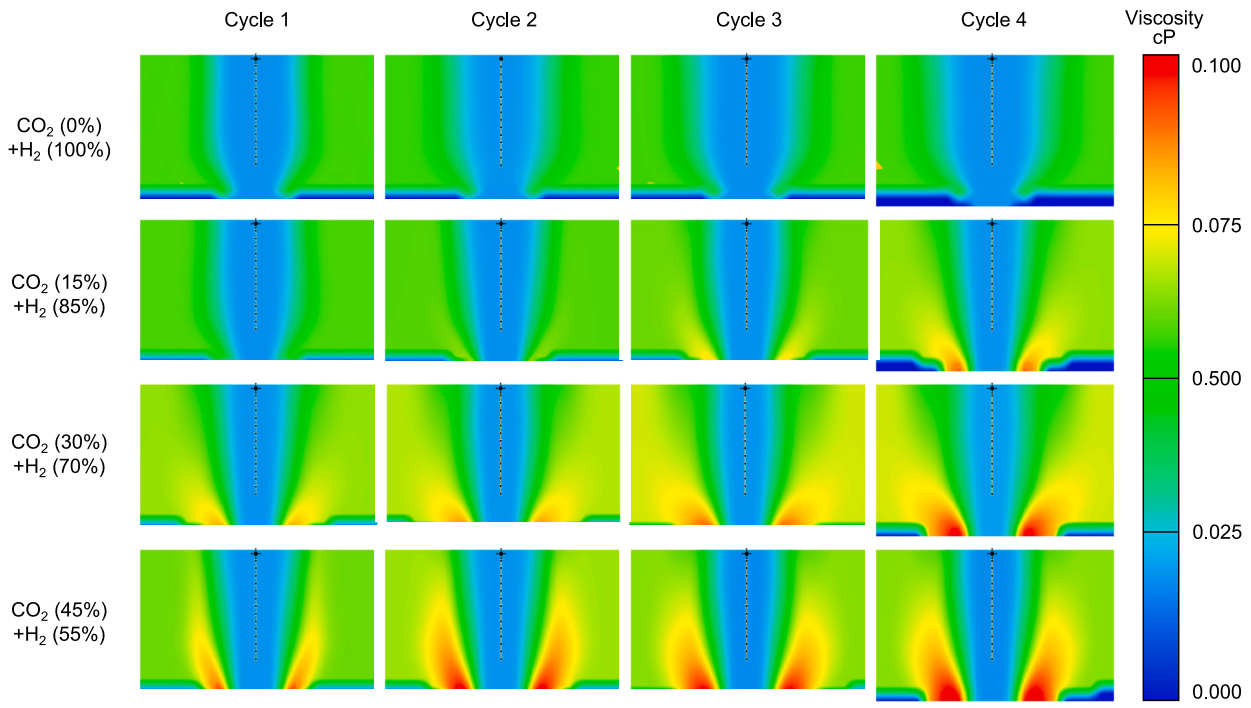

Fig. 16. Viscosity of hydrogen with CO_2 as cushion gas in mechanistic model.

strategies implemented ranged from the absence of cushion gas to the injection of CO_2 at varying proportions, including 15 %, 30 %, and 45 %. Since the primary goal of UHS is to manage seasonal fluctuations, with gas being injected during periods of low demand and production quickly during high demand, the cases design was based on a seasonal cycle of 6 months for injection followed by 6 months for production. For the entire UHS, both the hydrogen injection and production rates were set at 160 mln m^3/d. Additionally, key indicators including property distribution, gas supply stability, and water cut were evaluated over five cycles.

4.3.1. *Properties distribution*

The maps of properties, such as saturation, interfacial tension, and capillary force, for the Yakela UHS with different proportions of CO_2 injected, are shown in Fig. 17. With the introduction of CO_2, the region of high-concentration H_2 extends forward by 190 m compared to the case with no cushion gas injected (see Fig. 17(a)). A similar trend is noted in CO_2 saturation, which primarily distributes at the forefront of the hydrogen storage core area. When 45 % of CO_2 is injected, the maximum saturation of CO_2 can reach 88 % (see Fig. 17(b)). In the water saturation cross-section, a noticeable decrease in the water tongue of the hydrogen storage core area is observed with the injection of CO_2 cushion gas. This phenomenon is particularly evident in high-permeability areas, as shown on the steep left flank of the reservoir, where a thin interlayer with high permeability exists (see Fig. 17(c)). This indicates that the injection of CO_2 effectively reduces the effects of water intrusion in the UHS, thereby reducing the risk of increased water cut in the production well and even the risk of well shut-off.

Another noticeable impact of CO_2 is evident in the interfacial tension and capillary force profile (see Fig. 17(d) and Fig. 17(e)). As the amount of CO_2 increases, a distinct low interfacial tension region forms at the base of the Yakela's three layers. The interfacial tension in the hydrogen storage area decreases from 54 mN/m to 27 mN/m. Simultaneously, the capillary force profile shows a similar trend, dropping from 5 bar in the hydrogen storage zone to 2.3 bar within the CO_2 distribution area. These observations indicate that the protective zone established by CO_2 at the forefront of the hydrogen storage core significantly mitigates the potential for water intrusion into the hydrogen storage area.

On the relative permeability cross section, it is observed that without CO_2 injection, hydrogen can only achieve high relative permeability near the wellbore where hydrogen saturation is extremely high (see Fig. 17(f)). CO_2 injection enhances the seepage capability of the hydrogen storage area, elevating the relative permeability in the core region from 0.5 to 0.78. These characteristics suggest that CO_2 injection can optimize the reservoir's seepage environment, thereby augmenting the flow capacity of hydrogen in the UHS, which enables more efficient injection and extraction processes.

Furthermore, the CO_2 concentration also significantly influences the stability of the isolation zone. When CO_2 injection ranges from 0 % to 45 %, the isolation zone gradually expands, as indicated by the green zone in the four subplots of Fig. 17(b). When 30 % of CO_2 is injected, a sufficiently large isolation zone is formed, in which the analyzed parameters decrease and water saturation is lowered.

The density and viscosity profiles reveal the formation of a high-density, high-viscosity region at the forefront of the hydrogen storage area, characterized by an average density of 532 kg/m^3 and an average viscosity of 0.072 cP (see Fig. 17(g) and Fig. 17(h)). This region serves to impede the water intrusion from both sides of the reservoir and prevents its flow into the core of the hydrogen zone, thereby mitigating its effect on the core area. The cumulative effect of these mechanisms boosts the production stability of the UHS and curtails water intrusion.

4.3.2. *Storage efficiency*

The Yakela UHS's storage efficiency parameters, including H_2 production rate, purity, CO_2 content, and water cut were simulated in this study, as shown in Fig. 18. The injected CO_2 contributed significantly to stabilizing the storage zone during the production cycles, resulting in improved production rates and stable production capacity. As shown in Fig. 18(a), the last month of each cycle shows a rapid decline in production rates in the case without CO_2. In the first cycle without CO_2 injection, the H_2 production rate decreased by 72.5 %, compared to a 52.6 % decrease with the 45 % CO_2 injection case. However, since CO_2 flows out with H_2, the CO_2 injection ratio is negatively correlated with H_2 purity, as shown in Fig. 18(b). When injecting without CO_2, the average H_2 purity reaches 94.37 %. As CO_2 injection increases, the

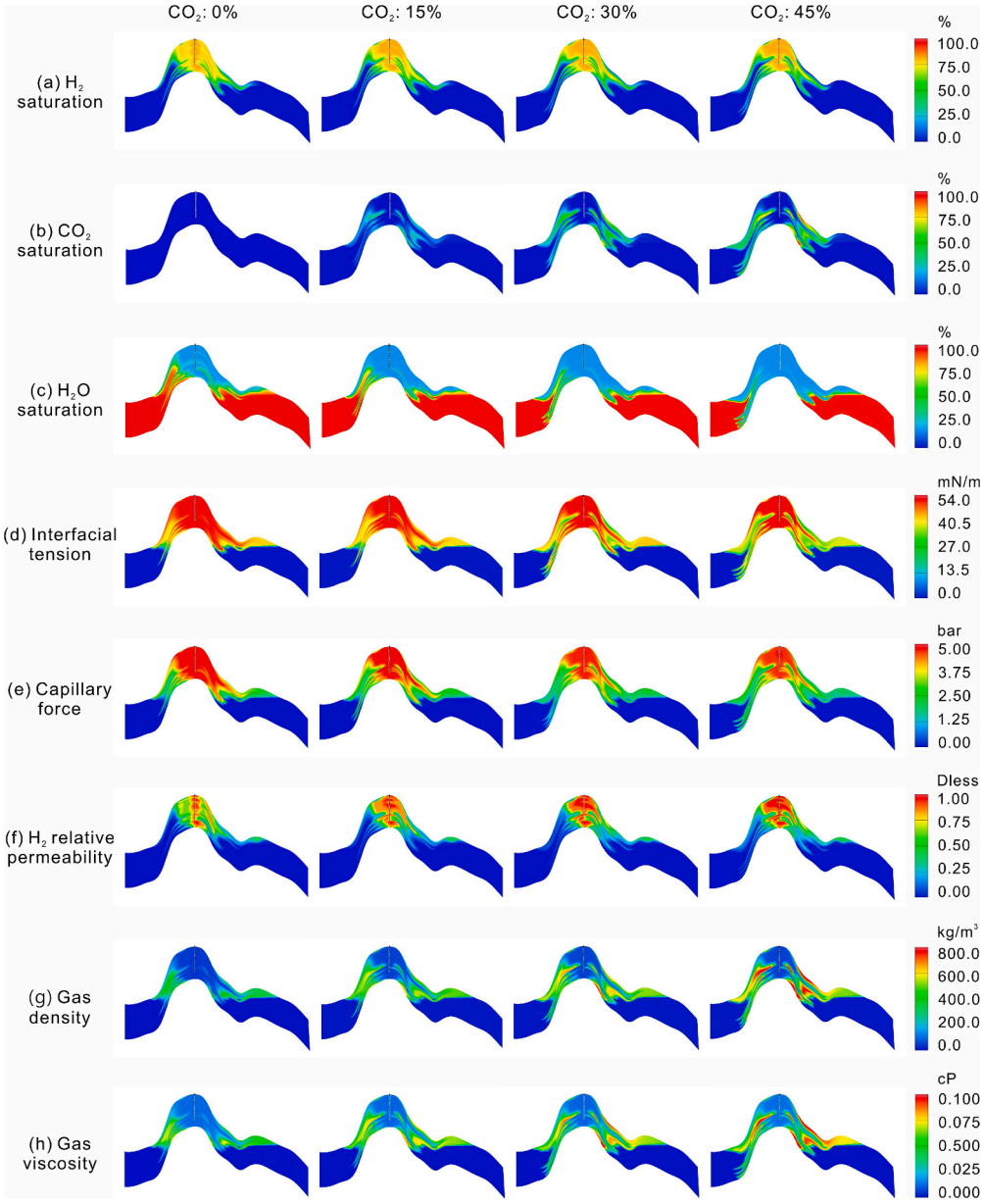

Fig. 17. Distribution cross-section of various properties after five cycles of gas injection in Yakela UHS.

average H_2 purity decreases, falling to 80.6 % when CO_2 injection reaches 45 %.

The CO_2 production ratio in different cases is shown in Fig. 18(c). In the initial cycle, the CO_2 production ratio is positively correlated with the injection amount. In the case with 45 % CO_2 injection, the CO_2 production ratio have reach 30.7 %. Moreover, as the production cycle progresses, the ratio gradually stabilizes at around 5.2 %. Additionally, due to the presence of CO_2 in the reservoir, even without CO_2 injection, approximately 0.43 % CO_2 is produced. This suggests that additional purification equipment is required to enhance the hydrogen purity in UHS.

Water cut is a key factor affecting the operations of large-scale UHS facilities. An increase in water cut indicates inadequate control over water intrusion or the presence of high-speed flow channels for bottom water. A continuous increase in water cut during gas well production can lead to sudden water breakthroughs, eventually leading to the closure of wells. In the simulation of the four production cases in Yakela UHS, without CO_2 cushion gas injection, the water cut of the produced gas consistently increases, rising from 28.2 % to 30.5 % over five cycles, see Fig. 18(d). However, water cut decreases significantly with CO_2 injection. Introducing a mere 15 % CO_2 is enough to halve the water content, and with a 30 % CO_2 injection, the average water cut over five cycles can be held at 11.7 %. Such a water cut level indicates effective control of water intrusion within the UHS, thereby promoting consistent H_2 production.

4.3.3. *Storage capacity*

The storage capacity, including the well downhole pressure, H_2 recovery factor, purity, and maximum production rate is shown as follows. The storage capacity is highly correlated with the downhole pressure. Due to the rock fracture pressure and fracture reactivation pressure limits, the UHS upper injection pressure should be below 620 bar. Thus, the maximum injection H_2 volumes are 810, 900, and 990 million m^3 for the 15 %, 30 %, and 45 % CO_2 injection cases, respectively, as shown in Fig. 19(a). As shown in Fig. 19(b), an increase in injection volume also leads to higher H_2 production rates, particularly in cases with CO_2 injection, where the hydrogen production rate increases from 3.29 mln m^3/d to 4.68 mln m^3/d, representing a 42.4 % increase. In cases without

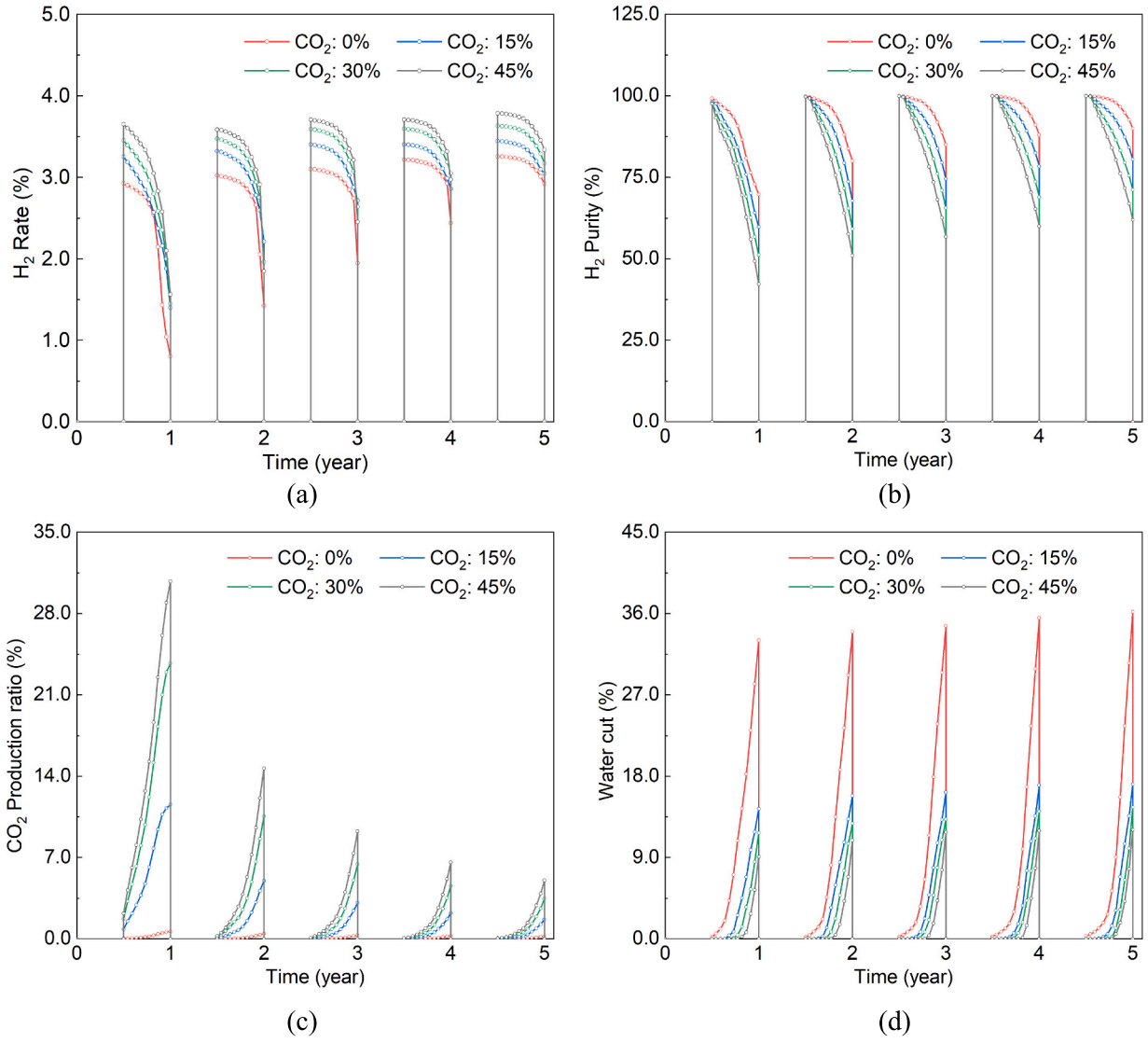

Fig. 18. Storage efficiency parameters under different CO_2 cushion gas volumes. (a) H_2 production rate. (b) H_2 purity. (c) CO_2 production content. (d) water cut.

CO_2 injection, a similar trend is observed, with the production rate rising from 2.1 mln m^3/d to 2.9 mln m^3/d, showing a 34.7 % increase.

The storage capacity increase helps suppress edge water in the reservoir, and the flow environment improves. As shown in Fig. 19(c), the H_2 recovery factor shows a rising trend with the injection volume, and the CO_2 injection ratio significantly influences the H_2 recovery factor. Without CO_2 injection, the recovery factor reaches a maximum of 71.2 %, even when the H_2 injection volume reaches 1080 million m^3. As a contrast, the recovery factor can reach up to 85.8 % with 810 million m^3 of H_2 when 45 % CO_2 is injected. The H_2 average purity in each cycle shows a weak positive correlation with the injection volume, as shown in Fig. 19(d). The maximum extent of average purity in different CO_2 ratio cases is only 4.08 %, which means that the storage capacity has little influence on the production purity.

4.4. Economic assessment

With the Yakela UHS production simulation results, a 30-year economic assessment has been conducted. The basic parameters for the assessment model are shown in Table 3.

where $ is USD, $M is USD million, MCM is million cubic meters, m is meter.

The Net Present Value (NPV) indicates a project's profitability by comparing the present value of cash inflow and outflow. It is the most significant parameter in economic assessment, as shown in Eq. (26) [56]. Considering the different ratios of cushion gas, the economic assessment results of Yakela UHS are shown in Fig. 20. With an increase in CO_2 content, the economic performance of UHS improves significantly primarily due to the enhanced hydrogen production from CO_2 injection, as shown in Fig. 20(a). When no CO_2 is injected, the NPV is only USD 52.52 million. However, with 15 % CO_2 injection, the NPV reaches USD 95.57 million, representing an 81.97 % increase in returns.

$$NPV = -CAPEX + \sum_{t=1}^{T} \frac{(C_{revenue} - OPEX - C_{tax})}{(1+r_d)^t} \quad (26)$$

where t is the year under calculation; T is the evaluation period for the entire project; $C_{revenue}$ is the revenue obtained from gas storage; C_{tax} is the tax levied by the government, calculated as 15 % of the total revenue; r_d is a discount rate.

The Internal Rate of Return (IRR) is the discount rate that makes the NPV of all cash flow equal to zero, as calculated in Eq. (27). The IRR also follows a similar trend as NPV, as shown in Fig. 20(b). When no CO_2 is injected, the IRR is 12.1 %, whereas with 30 % CO_2 injection, the IRR reaches 17.84 %. For a new energy storage project with a 30-year evaluation period, an IRR below 15 % is generally considered to have

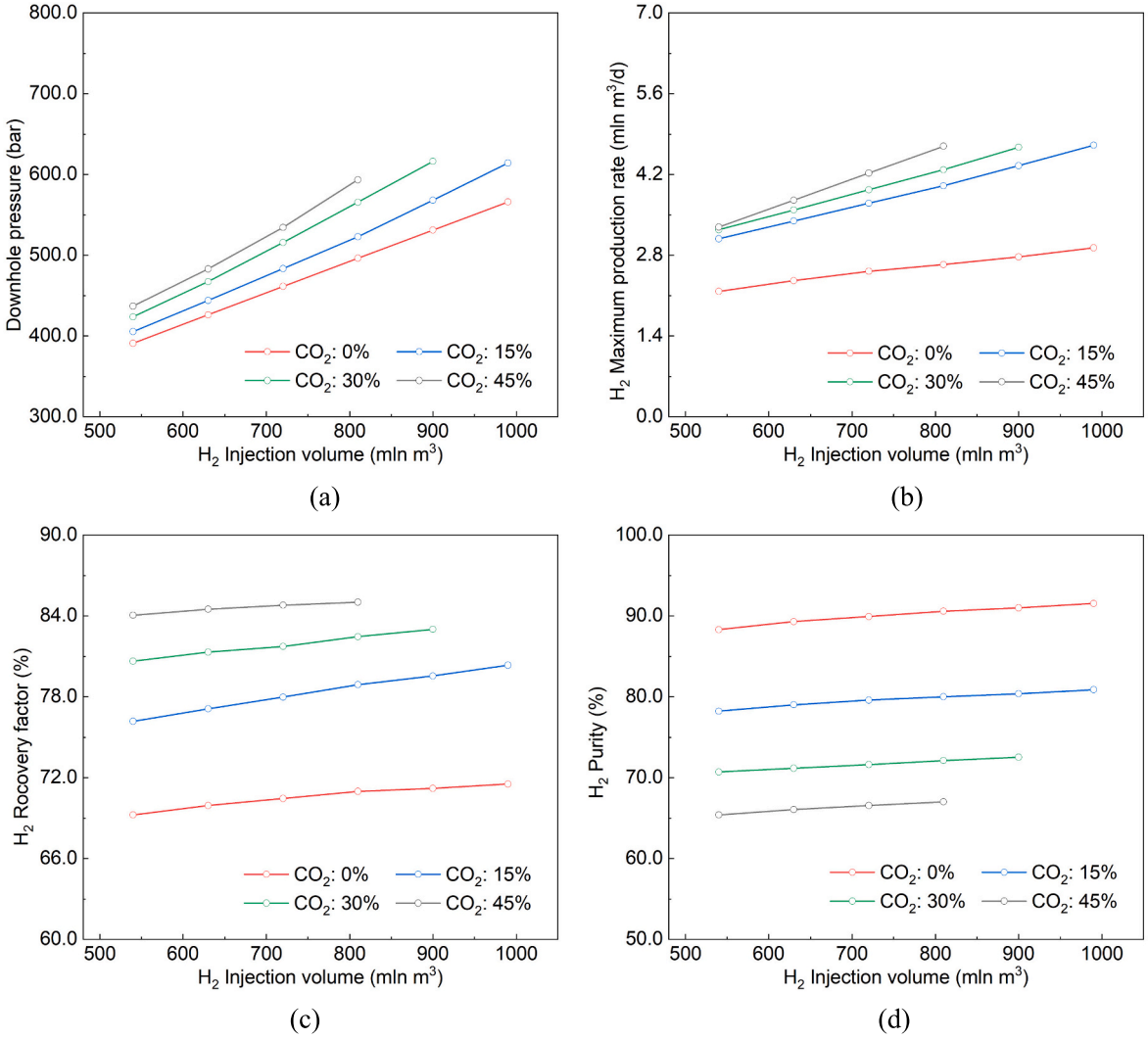

Fig. 19. Storage capacity parameters under different CO_2 cushion gas volumes. (a) H_2 recovery factor. (b) H_2 average purity in each cycle. (c) H_2 maximum production rate. (d) well downhole press.

Table 3
Basic parameters of economic assessment model.

Projects	Value	Projects	Value
CAPEX	$ 178.07 M	Cushion gas	90,000 ($/MCM)
Well drilling	726 ($/m)	CO_2 separation cost	78,600 ($/MCM)
Discount rate	10 %	Gas injection cost	23,900 ($/MCM)
Tax rate	15 %	Management cost	1720 ($/MCM)

limited investment appeal, underscoring the importance of CO_2 as a cushion gas in UHS.

$$NPV = \sum_{t=0}^{T} \frac{C_t}{(1+IRR)^t} \tag{27}$$

where *IRR* is the internal rate of return and C_t is the cash flow at year *t*.

5. Discussion

(1) Reservoir depth influence: Since deeper reservoirs experience higher pressures, resulting in greater pressure differentials and more energy release during hydrogen production, these conditions strongly influence the stability of the CO_2 protection zone. In the Yakela gas reservoir, which serves as a high-pressure case study, 30 % cushion gas was found to be sufficient. By contrast, shallower, lower-pressure reservoirs may require less CO_2 in UHS. However, the specific amount of CO_2 warrants further research because lower reservoir depth reduces temperature and pressure, thus decreasing critical CO_2 properties—such as density and viscosity—that maintain the stability of the protection zone.

(2) Water body energy influence: This study suggests that cushion gas primarily serves as a buffer between the aquifer and the core hydrogen storage area during repeated high-rate injection and production in UHS. Because water invasion occurs in most oil and gas reservoirs, the importance of cushion gas in UHS is particularly significant. Additionally, the required cushion gas volume can vary based on aquifer energy. For instance, the water body in the Yakela reservoir is estimated to be over 20 times the reservoir's size. Hence, in systems with smaller water bodies, the required CO_2 volume would likely be lower.

(3) Fracture influence: Fractures are commonly observed in gas reservoirs, and they can enhance reservoir permeability and gas production potential during the development phase. However, they may also cause rapid water breakthrough under UHS's cyclical high-rate injection and production. Therefore, reservoirs with multiple fractures would require more cushion gas to prevent intrusion into the core storage area.

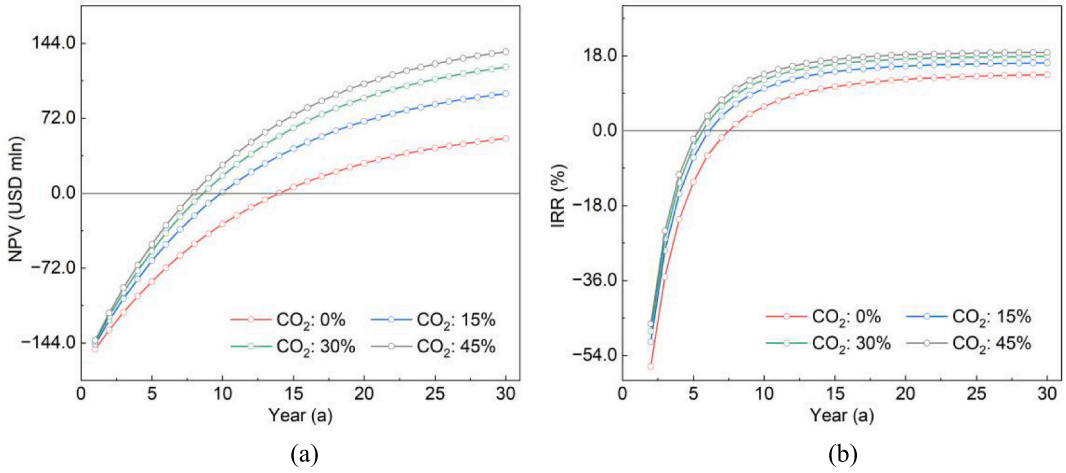

Fig. 20. Economic benefit of Yakela UHS. (a) NPV Model. (b) IRR Model.

(4) Potential variation of cushion gases: Apart from CO_2 used in this study, some researchers have examined the possibility of nitrogen, air, and natural gas serving as cushion gases in UHS. However, differences in flow characteristics between hydrogen and these gases have not been thoroughly analyzed, nor has the stability of the cushion gas isolation layer been quantitatively assessed. Consequently, these alternatives warrant further investigation regarding their potential and practical efficiency as cushion gases.
(5) Influence of methanogens: Methanogens are a type of anaerobic microorganism found in some reservoirs. The reaction between CO_2 and H_2 results in methane formation, which may consume hydrogen stored in the UHS. Considering that methanogens generally thrive in a temperature range of 30 °C to 60 °C, this study recommends conducting water sampling for microbial community analysis in UHS reservoirs shallower than 2000 m. If the methanogen content is high, the use of CO_2 as a cushion gas should be approached with caution. For deeper reservoirs (exceeding 2000 m), this step is not necessary.

6. Conclusions

This research employs a pore network model and numerical simulations to examine the risks associated with large-scale seasonal UHS, incorporating a mechanistic analysis. Additionally, it investigates the use of CO_2 as a cushion gas in Yakela UHS. The main conclusions reached are as follows:

(1) Hydrogen, characterized by its high interfacial tension and capillary force, presents a pronounced risk of large-scale water intrusion during multi-cycle injection-production patterns in UHS. This intrusion risk could potentially result in a significant decrease in the efficiency of gas storage operations.
(2) The use of CO_2 as a cushion gas can establish a high-density, high-viscosity protective zone. This approach reduces the interfacial tension and capillary force at the hydrogen storage forefront, thereby enhancing relative permeability, minimizing the risk of water intrusion, stabilizing hydrogen production from the wells, and significantly decreasing the water content.
(3) Traditional numerical simulations of UHS neglected to distinguish the unique characteristics, including interfacial tension, capillary force, and relative permeability curves, between hydrogen and CO_2. Such a simplified approach could potentially result in underestimating the advantages of CO_2 utilization as a cushion gas, based on its mechanism.
(4) The effectiveness of CO_2 as cushion gas in UHS is influenced by factors such as pressure, temperature, and an aquifer. As depth increases, higher reservoir pressure raises the risk of disrupting a CO_2 protective zone; however, the increased density and viscosity of CO_2 at greater depths contribute to the stability of the protective zone. Given the high investment costs of UHS projects, it is recommended to conduct numerical simulations based on specific geological conditions, together with the H_2 and CO_2 properties derived from this study.

CRediT authorship contribution statement

Peng Deng: Formal analysis, Data curation, Conceptualization. **Haoming Ma:** Methodology, Investigation. **Jinghan Song:** Validation, Software. **Xiaolong Peng:** Writing – review & editing, Supervision. **Suyang Zhu:** Resources, Project administration. **Dan Xue:** Formal analysis. **Liangliang Jiang:** Validation, Methodology. **Zhangxin Chen:** Supervision.

Declaration of competing interest

The authors declare that they have no known competing financial interests or personal relationships that could have appeared to influence the work reported in this paper.

Acknowledgements

This research has been made possible by contributions from the Natural Sciences and Engineering Research Council (NSERC)/Energi Simulation Industrial Research Chair in Reservoir Simulation, the Alberta Innovates (iCore) Chair in Reservoir Modeling, the Energi Simulation/Frank and Sarsh Meyer Collaboration Centre. “Central Government Guides Local Science and Technology Development” in Sichuan Provincial Department of Science and Technology [grant number 2022ZYD0003]. Sichuan Province Natural Science Fund for Youth [grant number 2023NSFSC0932]. National Natural Science Foundation of China (NSFC) Youth Fund [grant number 52104036].

Data availability

Data will be made available on request.

References

[1] The Paris Agreement: United Nations; 2015.
[2] Rogelj J, Den Elzen M, Hohne N, Fransen T, Fekete H, Winkler H, et al. Paris agreement climate proposals need a boost to keep warming well below 2 centigrade. Nature 2016;534:631–9.
[3] Vives AMV, Wang R, Roy S, Smallbone A. Techno-economic analysis of large-scale green hydrogen production and storage. Appl Energy 2023;346:121333.
[4] Brändle G, Schönfisch M, Schulte S. Estimating long-term global supply costs for low-carbon hydrogen. Appl Energy 2021;302:117481.
[5] Davis SJ, Lewis NS, Shaner M, Aggarwal S, Arent D, Azevedo IL, et al. Net-zero emissions energy systems. Science 2018;360:eaas9793.
[6] Mahlia TMI, Saktisahdan TJ, Jannifar A, Hasan MH, Matseelar HSC. A review of available methods and development on energy storage; technology update. Renew Sust Energ Rev 2014;33:532–45.
[7] Mahdi DS, Al-Khdheeawi EA, Yuan Y, Zhang Y, Iglauer S. Hydrogen underground storage efficiency in a heterogeneous sandstone reservoir. Advances in geo-energy. Research 2021:5.
[8] Chai M, Chen Z, Nourozieh H, Yang M. Numerical simulation of large-scale seasonal hydrogen storage in an anticline aquifer: a case study capturing hydrogen interactions and cushion gas injection. Appl Energy 2023;334:120655.
[9] Guerra K, Gutiérrez Alvarez R, Guerra OJ, Haro P. Opportunities for low-carbon generation and storage technologies to decarbonise the future power system. Appl Energy 2023;336:120828.
[10] IEA. The future of hydrogen. Paris International Energy Agency (IEA); 2019.
[11] U.S.. Natural gas total consumption. Washington, DC: U.S. Energy Information Administration; 2024.
[12] Ma XH. Handbook of underground gas storages and technology in. China: Springer; 2022.
[13] Lankof L, Urbanczyk K, Tarkowski R. Assessment of the potential for underground hydrogen storage in salt domes. Renew Sust Energ Rev 2022;160:112309.
[14] Shi KY, Chen JQ, Pang XQ, Jiang FJ, Hui SS, Zhang SJ, et al. Average molecular structure model of shale kerogen: experimental characterization, structural reconstruction, and pyrolysis analysis. Fuel 2024;355:129474.
[15] Bredesen K. Assessing rock physics and seismic characteristics of the Gassum formation in the Stenlille aquifer gas storage: a reservoir analog for the Havnsø CO2 storage prospect, Denmark. Int J Greenhouse Gas Control 2022;114:103583.
[16] Raad SMJ, Leonenko Y, Hassanzadeh H. Hydrogen storage in saline aquifers: opportunities and challenges. Renew Sust Energ Rev 2022;168:112846.
[17] Pan B, Liu K, Ren B, Zhang M, Ju Y, Gu J, et al. Impacts of relative permeability hysteresis, wettability, and injection/withdrawal schemes on underground hydrogen storage in saline aquifers. Fuel 2023;333:126516.
[18] Wang H, Chen SN, Deng P, Wang MM, Xu ZX. Pore-scale investigation of caprock integrity in underground hydrogen storage. In: SPE Canadian Energy Technology Conference: SPE; 2024. p. D021S6R05.
[19] Liu J, Zhang T, Sun SY. Molecular mechanisms of hydrogen leakage through caprock in moisture and residual gas conditions: a molecular dynamics–Monte Carlo study. Phys Fluids 2024;36.
[20] IEA. Global hydrogen review. Paris; 2022.
[21] Heinemann N, Alcalde J, Miocic JM, Hangx SJT, Kallmeyer J, Ostertag Henning C, et al. Enabling large-scale hydrogen storage in porous media – the scientific challenges. Energy Environ Sci 2021;14:853–64.
[22] Ma HM, Yang Y, Zhang YM, Li ZY, Zhang K, Xue ZQ, et al. Optimized schemes of enhanced shale gas recovery by CO2-N2 mixtures associated with CO2 sequestration. Energy Convers Manag 2022;268:116062.
[23] Hematpur H, Abdollahi R, Rostami S, Haghighi M. Blunt MJ. Review of Underground Hydrogen Storage: Concepts and challenges. Advances in Geo-Energy Research; 2023. p. 7.
[24] Haynes WM. CRC handbook of chemistry and physics: CRC press; 2016.
[25] Di CJ, Wei YZ, Wang K, Deng P, Chen B, Shen LH, et al. The impact of pressurization-induced decrease of capillary pressure and residual saturation on geological carbon dioxide storage. J Clean Prod 2024;144573.
[26] Ahmed T. Reservoir engineering handbook. Gulf Professional Publishing; 2018.
[27] Adam KM, Bloomsburg GL, Corey AT. Diffusion of trapped gas from porous media. Water Resour Res 1969;5:840–9.
[28] Gessel SV, Hajibeygi H. Hydrogen TCP-task 42 (2023), "underground hydrogen storage: Technology monitor report". Paris: IEA; 2023. p. 153.
[29] Ma JF, Li L, Wang HF, Du Y, Ma JJ, Zhang XL, et al. Carbon capture and storage: history and the road ahead. Engineering0 2022;14:33–43.
[30] Zhang ZE, Wang T, Blunt MJ, Anthony EJ, Park AHA, Hughes RW, et al. Advances in carbon capture, utilization and storage. Appl Energy 2020;278:115627.
[31] Sherif SA, Goswami DY, Stefanakos EL, Steinfeld A. Handbook of Hydrogen Energy: CRC press; 2014.
[32] Kanaani M, Sedaee B, Asadian-Pakfar M. Role of cushion gas on underground hydrogen storage in depleted oil reservoirs. J Energy Storage 2022;45:103783.
[33] Bo ZK, Hörning S, Underschultz JR, Garnett A, Hurter S. Effects of geological heterogeneity on gas mixing during underground hydrogen storage (UHS) in braided-fluvial reservoirs. Fuel 2024;357:129949.
[34] Wang G, Pickup G, Sorbie K, Mackay E. Numerical modelling of H2 storage with cushion gas of CO2 in subsurface porous media: filter effects of CO2 solubility. Int J Hydrog Energy 2022;47:28956–68.
[35] Shi KY, Chen JQ, Pang XQ, Jiang FJ, Hui SS, Zhao ZC, et al. Wettability of different clay mineral surfaces in shale: implications from molecular dynamics simulations. Petrol Sci 2023;20:689–704.
[36] Huang T, Moridis GJ, Blasingame TA, Abdulkader AM, Yan B. Compositional reservoir simulation of underground hydrogen storage in depleted gas reservoirs. Int J Hydrog Energy 2023;48:36035–50.
[37] Andersen O, Nilsen HM. Investigating simplified modeling choices for numerical simulation of CO2 storage with thermal effects. Int J Greenhouse Gas Control 2018;72:49–64.
[38] Kumar A, Ozah R, Noh M, Pope GA, Bryant S, Sepehrnoori K, et al. Reservoir simulation of CO2 storage in deep saline aquifers. SPE J 2005;10:336–48.
[39] Li S, Zhang Y, Zhang X. A study of conceptual model uncertainty in large-scale CO2 storage simulation. Water Resour Res 2011;47.
[40] Zhao QQ, Wang YH, Chen C. Numerical simulation of the impact of different cushion gases on underground hydrogen storage in aquifers based on an experimentally-benchmarked equation-of-state. Int J Hydrog Energy 2024;50:495–511.
[41] Gostick J, Aghighi M, Hinebaugh J, Tranter T, Hoeh MA, Day H, et al. OpenPNM: a pore network modeling package. Comput Sci Eng 2016;18:60–74.
[42] Joekar Niasar V, Hassanizadeh SM. Analysis of fundamentals of two-phase flow in porous media using dynamic pore-network models: a review. Crit Rev Environ Sci Technol 2012;42:1895–976.
[43] Chen ZX. Reservoir simulation: mathematical techniques in oil recovery. Soc Ind Appl Math. 2007. p. 157–76.
[44] Zhang NL, Luo ZF, Chen ZX, Liu FS, Liu PL, Chen WY, et al. Thermal–hydraulic–mechanical–chemical coupled processes and their numerical simulation: a comprehensive review. Acta Geotech 2023;1-22.
[45] Chen ZX, Huan GR, Ma YL. Computational methods for multiphase flows in porous media: Society for Industrial and Applied Mathematics. 2006. p. 22–47.
[46] Lopez Echeverry JS, Reif Acherman S, Araujo Lopez E. Peng-Robinson equation of state: 40 years through cubics. Fluid Phase Equilib 2017;447:39–71.
[47] Song YL, Song ZJ, Chen ZX, Zhang LC, Zhang YF, Feng D, et al. Fluid phase behavior in multi-scale shale reservoirs with nano-confinement effect. Energy 2024;289:130027.
[48] Deng P, Chen ZX, Peng XL, Wang JF, Zhu SY, Ma HM, et al. Optimized lower pressure limit for condensate underground gas storage using a dynamic pseudo-component model. Energy 2023;285:129505.
[49] Peng DY, Robinson DB. A new two-constant equation of state. Ind Eng Chem Fundam 1976;15:59–64.
[50] Jia C, Wei G. Structural characteristics and petroliferous features of Tarim Basin. Chin Sci Bull 2002;47:1–11.
[51] Song DF, Wang TG, Li HB. Geochemical characteristics and origin of the crude oils and condensates from Yakela faulted-uplift, Tarim Basin. J Pet Sci Eng 2015;133:602–11.
[52] Map of China. Ministry of Natural Resources of the People's Republic of China: Standard map service system2025.
[53] Firoozabadi A, Ramey Jr HJ. Surface tension of water-hydrocarbon systems at reservoir conditions. J Can Petrol Technol 1988;27.
[54] Lee AL, Gonzalez MH, Eakin BE. The viscosity of natural gases. J Pet Technol 1966;18:997–1000.
[55] Heidaryan E, Aryana SA. Empirical correlations for density, viscosity, and thermal conductivity of pure gaseous hydrogen. Advances in geo-energy. Research 2024:11.
[56] Samuelson P. Foundations of economic analysis. Harvard University Press; 1983.
[57] Qian Z, Deng P, Qu BC, et al. Gel plugging simulation with a new model and applications[J]. Phys. Fluids 2025;37(1). https://doi.org/10.1063/5.0248648.